Numerical Investigation of Rarefied Hypersonic Flows over Flying Configurations Using a Nonlinear Constitutive Model

Zhongzheng Jiang,[*] Wenwen Zhao,[†] Zhenyu Yuan,[‡] and Weifang Chen[§]

College of Aeronautics and Astronautics, Zhejiang University, Hangzhou, China, 310027

and

R.S. Myong[¶]

Department of Aerospace and Software Engineering and ACTRC & ReCAPT, Gyeongsang National University, Jinju, Gyeongnam 52828, South Korea

The linear Navier-Stokes-Fourier (NSF) constitutive relations are derived on the assumption of the small deviation from local thermodynamic equilibrium, and consequently they may fail in describing flows removed far from local equilibrium, like rarefied hypersonic flows. In this paper, a nonlinear constitutive model of diatomic gases named as nonlinear coupled constitutive relations (NCCR) is presented. The model conceptually starts from Eu's generalized hydrodynamics and is developed for simulating rarefied hypersonic gas flows with a goal of recovering NSF's solutions in near-continuum regime and more accurate in transition regime. To enhance stable computation, an undecomposed algorithm is further developed

Presented as Paper 2017-2346 at the 21st AIAA International Space Planes and Hypersonic Systems and Technology Conference, Xiamen, China, 6-9 March 2017.

*Research Associate, College of Aeronautics and Astronautics, Zhejiang University, Hangzhou, China, 310027; Senior Member, AIAA; jzhongzh@zju.edu.cn.

†Associate Professor, College of Aeronautics and Astronautics, Zhejiang University, Hangzhou, China, 310027; Senior Member, AIAA; wwzhao@zju.edu.cn (Corresponding Author).

‡ Ph.D. candidate, College of Aeronautics and Astronautics, Zhejiang University, Hangzhou, China, 310027; yuanzhenyu318@zju.edu.cn.

§Professor, College of Aeronautics and Astronautics, Zhejiang University, Hangzhou, China, 310027; chenwfnudt@zju.edu.cn.

¶Professor, Department of Aerospace and Software Engineering and ACTRC & ReCAPT, Gyeongsang National University, Jinju, Gyeongnam 52828, South Korea; Associate Fellow, AIAA; myong@gnu.ac.kr.

for the nonlinear constitutive model within finite volume framework. An analysis is carried out to compare the algorithm with Myong's original decomposed algorithm. Local non-equilibrium flow regions are also investigated for rarefied hypersonic flows over a cone tip, a hollow cylinder-flare and a HTV-type flying vehicle. The convergent solutions of NCCR model are compared with NSF, DSMC calculations and experimental data. It is demonstrated from results of general flow-field and surface properties that the NCCR model is as computationally efficient as the NSF model in continuum regime, and, at the same time, more accurate in comparison with DSMC and experimental data than NSF in non-equilibrium flows.

Nomenclature

C = peculiar velocity (m/s)

$\Phi^{(k)}$ = macroscopic variables

$h^{(k)}$ = molecular expressions for macroscopic variables

f = phase density

k_B = Boltzmann constant

μ = normalization factor in Eu's phase density

d = molecular diameter

d_{ref} = reference molecular diameter

c = NCCR constant $\left(mk_BT_r\right)^{1/4} \Big/ 2d_r\eta_r^{1/2}$

m = molecular mass

E = total energy per unit mass (J/kg)

$\hat{\mathbf{F}}_c, \hat{\mathbf{G}}_c, \hat{\mathbf{H}}_c$ = convective flux vector

$\hat{\mathbf{F}}_v, \hat{\mathbf{G}}_v, \hat{\mathbf{H}}_v$ = viscous flux vector

$\mathbf{A}^{\pm}, \mathbf{B}^{\pm}, \mathbf{C}^{\pm}$ = inviscid approximate Jacobian matrixes

$\xi_x, \xi_y, \xi_z, \xi_t, \eta_x, \eta_y, \eta_z, \eta_t, \zeta_x, \zeta_y, \zeta_z, \zeta_t$ = metrics

$\rho(\mathbf{A}), \rho(\mathbf{B}), \rho(\mathbf{C})$ = spectral radiuses for the inviscid Jacobian matrixes.

$\hat{\mathbf{Q}}$ = vector of flow variables in physical domain

J = Jacobian coordinate

Kn_{BLG} = the body-length global (BLG) Knudsen number

L = characteristic length (m)

L_0 = reference length (m)

l_∞ = mean free path of gas molecules (m)

Ma = Mach number

Re = Reynolds number

N_δ = ratio of Mach number to Reynolds number

Pr = Prandtl number

p = pressure (N/m^2)

p_∞ = free-stream pressure (N/m^2)

T = temperature (K)

T_∞ = free-stream temperature (K)

T_{ref} = reference temperature (K)

T_w = wall temperature

α = attack angle

U_∞ = free-stream velocity (m/s)

u_i = velocity components (m/s)

ρ = density (kg/m^3)

ρ_∞ = free-stream density (kg/m^3)

ρ_{ref} = reference density (kg/m^3)

η = viscosity ($(N \cdot s)/m^2$)

η_{ref} = reference viscosity ($(N \cdot s)/m^2$)

η_b = bulk viscosity ($(N \cdot s)/m^2$)

λ = thermal conductivity ($J/(m \cdot s \cdot K)$)

f_b = ratio of the bulk viscosity to the shear viscosity

s_{VHS} = VHS temperature exponent

R = gas constant ($J/(kg \cdot K)$)

γ = specific heat ratio

c_p = constant-pressure specific heat ($J/(kg \cdot K)$)

C_p = pressure coefficient

C_f = skin friction coefficient

C_h = heat transfer rate

$\mathbf{\Pi}$ = shear stress tensor (N/m^2)

Δ = excess normal stress (N/m^2)

$\mathbf{Q}$ = heat flux (w/ m^2)

ψ = higher-order moments

κ = first-order cumulant of cumulant expansion for dissipation terms

$q(\kappa)$ = nonlinear dissipation factor

$\hat{R}$ = dimensionless Rayleigh-Onsager dissipation function

$[\mathbf{A}]^{(2)}$ = traceless symmetric part of the second-rank tensor $\mathbf{A}$, equal to $\left(A + A^T\right)/2 - \mathbf{I}Tr\mathbf{A}/3$

$\mathbf{I}$ = identity matrix

I. Introduction

Gaseous flows in near space—defined as the airspace between 20 to 100 kilometres high above sea level—have been investigated intensively in recent years. In near space, the physical properties of gas including the density and pressure vary as a function of altitude rather dramatically. Re-entry vehicles such as HTV

(Hypersonic Technology Vehicle), space shuttle or Apollo capsule, experience different flow features from continuum to transition regimes when passing through near space during the course of their flight trajectory. The local flow fields around hypersonic vehicles at high altitudes contain typical rarefied non-equilibrium characteristics, like the shock waves around the sharp leading edge, Knudsen layer near the solid surface, as well as the gaseous expansion region in the near-wake of vehicles. The reproduction of such non-equilibrium phenomena in ground-based facilities or flight tests is extremely challenging and expensive and thus numerical simulation should be considered an efficient choice for the design of such vehicles. However, as the rarefied non-equilibrium effects are strengthened, the validity of the linear laws of Navier-Stokes-Fourier (NSF) based on near-equilibrium becomes questionable. Hence a more refined theoretical tool beyond the classical theory of linear constitutive relations needs to be developed.

In the past, much effort has been placed on obtaining the physical solutions of the challenging flow problems beyond the capability of the linear NSF equations. Among them, the direct simulation Monte Carlo (DSMC) method [1] is considered most powerful in solving the Boltzmann (or equivalent) equations by counting the collisions of representative molecules with collision frequencies and scattering velocity distributions. Other well-known methods also include the linearized methods of Boltzmann equation [2], Boltzmann model equations (BGK, ES-BGK and Shakhov models) [3-5], discrete velocity methods (DVM) [6], unified gas-kinetic scheme(UGKS) [7], Burnett-type equations [8-10], Grad's moment equations [11], regularized 13 moment equations [12] etc. For prediction of aerodynamic characteristics of re-entry vehicles, it is recommended that any new methods should meet three standards: (1) recovering the Navier-Stokes-Fourier solution in continuum regime and extendable to the transition regime; (2) acceptable computational efficiency with reasonable cost; (3) capable of handling complex configurations. However, either huge computational cost or numerical instability when handling complex geometries makes most of the aforementioned methods less popular in engineering

application.

A set of generalized hydrodynamic equations proposed by Eu [13] in 1980 provides an alternative solution procedure to the Boltzmann equation. However, the Eu's 13 moment equations also have difficulty in handling multi-dimensional problems. In order to provide a practical high-order fluid dynamic model with computational efficiency comparable to that of the NSF model, Myong in 1999 developed an efficient computational model on the basis of Eu's generalized equations [14, 15]. The model, named as the nonlinear coupled constitutive relations (NCCR), takes a form of nonlinear algebraic system and can be implemented easily in the conservation laws. This second-order NCCR model derived from the kinetic Boltzmann equation via the so-called balanced closure was validated in the force-driven Poiseuille flow through the deterministic microscopic molecular dynamics (MD) method [16].

Myong employed a decomposed computational algorithm to numerically solve the implicit algebraic nonlinear model, which was applied successfully in one-dimensional shock wave structure and multi-dimensional flows [14, 17]. Nonetheless, there is still a room for improving the iterative numerical method from decomposed to undecomposed in order to enhance the numerical stability and accuracy, in particular, for three-dimensional complicated flow problems in case of finite volume framework [18, 19]. In present work, we attempt to utilize a hybrid algorithm which combined fixed-point and Newton's iterations for computing non-conserved variables in implicit NCCR model in conjunction with modern CFD schemes to solve the conservation laws for conserved variables within finite volume framework. The hybrid method is then applied to solve several hypersonic flows over flying configurations. A brief introduction of the nonlinear constitutive model and the numerical method is given in Section II and III. Section IV will discuss the general flow-field and surface properties computed by the new model and present a detailed comparison with the linear NSF, DSMC and experimental results. It will be demonstrated that the present computational model is as efficient as the NSF

model in continuum regime, and, at the same time, more accurate in comparison with DSMC and experimental data than NSF in non-equilibrium flows considered.

II. A Nonlinear Constitutive Model of Diatomic Gases

In order to solve the far-from-equilibrium flow problems, Eu [20, 21] developed the generalized hydrodynamic equations (GHE) compatible with the second laws of thermodynamics. Different from Chapman-Enskog expansion with Knudsen number as a small parameter, GHE was derived from the kinetic Boltzmann-Curtiss equation by introducing a non-equilibrium canonical distribution function in exponential form and the cumulant-expansion method for modelling the collision term. The Eu's non-equilibrium canonical distribution function is defined as

$$f = \exp\left[-\frac{1}{k_B T}\left(\frac{1}{2}mC^2 + H_{rot} + \sum_{k=1}^{\infty} X_k h^{(k)} - \mu\right)\right], \tag{1}$$

In (1), C denotes the peculiar velocity and μ is the normalization factor. X_k are the functions of macroscopic variables, occupying the status similar to the coefficients of Maxwell-Grad moment method. T, k_B, m and H_{rot} represent the temperature, Boltzmann constant, molecular mass and rotational Hamiltonian of molecule, respectively. $h^{(k)}$ denotes the molecular expressions for macroscopic variables. For the conserved or non-conserved variables, like the mass density ρ, momentum density $\rho\mathbf{u}$, energy density ρe, or the shear stress $\mathbf{\Pi}$, excess normal stress Δ, heat flux $\mathbf{Q}$, their corresponding molecular expressions can be defined respectively as

$$\begin{aligned} &h^{(1)} = m,\ h^{(2)} = m\mathbf{v},\ h^{(3)} = 1/2\, mC^2 + H_{rot}, h^{(4)} = [m\mathbf{CC}]^{(2)}, \\ &h^{(5)} = \frac{1}{3}mC^2 - p/n,\ \ h^{(6)} = (\frac{1}{2}mC^2 + H_{rot} - \hat{h}m)\mathbf{C}, \end{aligned} \tag{2}$$

where $\mathbf{v}$, p, n and $\hat{h}$ represent the particle velocity, pressure, number density of molecules and the enthalpy density per unit mass respectively. The square bracket symbol $[\mathbf{A}]^{(2)}$ in (2) represents the

traceless symmetric part of the second-rank tensor $\mathbf{A}$. The shear stress $\mathbf{\Pi}$, the excess normal stress Δ and the pressure p constitute the stress tensor $\mathbf{P}$ through the following relation

$$\mathbf{P} = \left(p + \Delta \right)\mathbf{I} + \mathbf{\Pi},$$

where $\mathbf{I}$ denotes the unit second-rank tensor.

The aforementioned macroscopic variables $\Phi^{(k)}$ can be computed by integrating the product of their molecular expressions $h^{(k)}$ and the distribution function over the whole velocity space

$$\Phi^{(k)} = \int h^{(k)} f d\mathbf{v}. \tag{3}$$

Differentiating the variables (3) with time and employing the Boltzmann-Curtiss equation, a set of evolution equations for the macroscopic variables can be derived as

$$\rho \frac{d\left(\Phi^{(k)} / \rho \right)}{dt} + \nabla \cdot \psi^{(k)} = \Lambda_k + Z_k, \tag{4}$$

where $\psi^{(k)}$, Λ_k and Z_k denote the flux of high-order moments, the dissipation term and the kinematic term respectively. Using Eu's non-equilibrium canonical distribution function to close the dissipation term, a set of evolution equations of non-conserved variables for a diatomic gas (GHE) can be finally obtained as

$$\begin{aligned}
&\rho \frac{D\left(\mathbf{\Pi}/\rho \right)}{Dt} + \nabla \cdot \psi_4 = -2\left[\mathbf{\Pi} \cdot \nabla \mathbf{u} \right]^{(2)} - \frac{p}{\eta} \mathbf{\Pi} q\left(\kappa \right) - 2(p + \Delta)\left[\nabla \mathbf{u} \right]^{(2)}, \\
&\rho \frac{D\left(\Delta/\rho \right)}{Dt} + \nabla \cdot \psi_5 = -2\gamma'(\Delta \mathbf{I} + \mathbf{\Pi}) : \nabla \mathbf{u} - \frac{2}{3}\gamma' p \nabla \cdot \mathbf{u} - \frac{2}{3}\gamma' \frac{p}{\eta_b} \Delta q\left(\kappa \right), \\
&\rho \frac{D\left(\mathbf{Q}/\rho \right)}{Dt} + \nabla \cdot \psi_6 + \psi_3 : \nabla \mathbf{u} = -\mathbf{\Pi} \cdot c_p \nabla T - \mathbf{Q} \cdot \nabla \mathbf{u} - (p + \Delta) c_p T \nabla \ln T + \nabla \cdot \left[(p + \Delta)\mathbf{I} + \mathbf{\Pi} \right] \cdot \frac{(\mathbf{\Pi} + \Delta \mathbf{I})}{\rho} - \frac{p c_p}{\lambda} \mathbf{Q} q\left(\kappa \right).
\end{aligned} \tag{5}$$

In equations (5), γ' is equal to $(5 - 3\gamma)/2$. $\psi_{3,4,5,6}$, c_p, η, η_b and λ represent the flux of high-order moments, the constant-pressure specific heat, and the coefficients of the gas viscosity, the bulk viscosity, the heat conduction respectively. The nonlinear dissipation factor $q\left(\kappa \right) = \sinh\left(\kappa \right)/\kappa$ with

$$\kappa = \left(m k_B T \right)^{1/4} \Big/ \sqrt{2} d p \left[\mathbf{\Pi} : \mathbf{\Pi} / 2\eta + \gamma' \Delta^2 / \eta_b + \mathbf{Q} \cdot \mathbf{Q} / \lambda T \right]^{1/2}$$

affects the relaxation times of non-conserved variables as a non-equilibrium coefficient in the evolution equations (5). In order to close aforementioned evolution equations, Eu [21, 22] proposed a simple closure based

on a heuristic consideration

$$\psi_3 = \psi_4 = \psi_5 = \psi_6 = 0.$$

Moreover, Myong [23] proposed another closure explanation, called as 'balanced closure', from a keen observation that the number of places for closing the moment equations is two, rather than one, as misleadingly described by the previous theory based on the Maxwellian molecule assumption. The order of approximations in handling two terms—kinematic (movement) and dissipation (collision) terms—must be the same accordingly, for instance, second-order for both terms, thus achieving a balance between the kinematic and collision term approximation, namely, the second-order closure for the kinematic terms,

$$\nabla \cdot \psi_4 = \nabla \cdot \psi_5 = \nabla \cdot \psi_6 + \psi_3 : \nabla \mathbf{u} = 0$$

while maintaining the same second-order closure for $q(\kappa)$.

In the case of the steady-state flow problems, the time terms of non-conserved variables in GHE may play a negligible role in the numerical computation. Thus the substantial time derivative terms $D(\mathbf{\Pi}/\rho)/Dt$, $D(\Delta/\rho)/Dt$ and $D(\mathbf{Q}/\rho)/Dt$ in the left hand side of GHE (5) in constitutive equation level can be ignored by an adiabatic approximation assumption introduced by Eu [21]. The transport of conserved variables and the non-conserved variables varies on two different time scales. The non-conserved variables change much faster than the conserved variables and thus reach a steady state very quickly than the latter. Therefore, on the time scale of conserved variables, the time terms for non-conserved variables can be neglected as a physically-motivated approximation. Note that the derivative term of non-conserved variables $\nabla \cdot \left[(p+\Delta)\mathbf{I} + \mathbf{\Pi}\right] \cdot (\mathbf{\Pi} + \Delta\mathbf{I})/\rho$ is removed by Myong in order to establish an algebraic (rather than partial differential) system which can be solved by iterative methods. The term $\mathbf{Q} \cdot \nabla \mathbf{u}$ is also omitted for the sake of simplicity [15, 17]. In our recent work [24, 25], the insignificant effect from this term has been confirmed in one-dimensional steady shock wave structures.

Finally, a nonlinear algebraic system of the second-order nonlinear model, namely the nonlinear coupled constitutive relations (NCCR), is developed. The NCCR model of diatomic gases can be summarized as

$$\begin{aligned}
&-2\left[\boldsymbol{\Pi}\cdot\nabla\mathbf{u}\right]^{(2)}-\frac{p}{\eta}\boldsymbol{\Pi}q\left(\kappa\right)-2(p+\Delta)\left[\nabla\mathbf{u}\right]^{(2)}=0,\\
&-2\gamma'(\Delta\mathbf{I}+\boldsymbol{\Pi}):\nabla\mathbf{u}-\frac{2}{3}\gamma' p\nabla\cdot\mathbf{u}-\frac{2}{3}\gamma'\frac{p}{\eta_b}\Delta q\left(\kappa\right)=0,\\
&-\boldsymbol{\Pi}\cdot c_p\nabla T-\frac{pc_p}{\lambda}\mathbf{Q}q\left(\kappa\right)-(p+\Delta)c_pT\nabla\ln T=0.
\end{aligned}\tag{6}$$

Note that the linear Navier-Stokes-Fourier constitutive relations, derived from the first-order Chapman-Enskog expansion, can be naturally recovered from the second-order model in vanishing Knudsen and Mach numbers,

$$\boldsymbol{\Pi}_0=-2\eta\left[\nabla\mathbf{u}\right]^{(2)},\quad \Delta_0=-\eta_b\nabla\cdot\mathbf{u},\quad \mathbf{Q}_0=-\lambda\nabla T.\tag{7}$$

It is worthwhile mentioning that the bulk viscosity is set zero in the linear theory according to the Stokes' hypothesis. After introducing the definition of NSF relations (7) into the NCCR model (6) and non-dimensionalizing with proper flow parameters [18], we can obtain another very compact form of the NCCR model as

$$\begin{aligned}
&\hat{\boldsymbol{\Pi}}q\left(c\hat{R}\right)=(1+\hat{\Delta})\hat{\boldsymbol{\Pi}}_0+\left[\hat{\boldsymbol{\Pi}}\cdot\nabla\hat{\mathbf{u}}\right]^{(2)},\\
&\hat{\Delta}q\left(c\hat{R}\right)=\hat{\Delta}_0+\frac{3}{2}f_b(\hat{\Delta}\mathbf{I}+\hat{\boldsymbol{\Pi}}):\nabla\hat{\mathbf{u}},\\
&\hat{\mathbf{Q}}q\left(c\hat{R}\right)=(1+\hat{\Delta})\hat{\mathbf{Q}}_0+\hat{\boldsymbol{\Pi}}\cdot\hat{\mathbf{Q}}_0,
\end{aligned}\tag{8}$$

where

$$\frac{\eta_\infty}{\rho_\infty a_\infty L_0}=N_\delta=\frac{\mathrm{Ma}}{\mathrm{Re}},\quad \hat{\boldsymbol{\Pi}}=\frac{N_\delta}{p}\boldsymbol{\Pi},\quad \hat{\Delta}=\frac{N_\delta}{p}\Delta,\quad \hat{\mathbf{Q}}=\frac{N_\delta}{p}\frac{\mathbf{Q}}{\sqrt{T/(2\varepsilon)}}$$

$$\hat{R}=\left[\hat{\boldsymbol{\Pi}}:\hat{\boldsymbol{\Pi}}+\frac{2\gamma'}{f_b}\hat{\Delta}^2+\hat{\mathbf{Q}}\cdot\hat{\mathbf{Q}}\right]^{1/2},\nabla\hat{\mathbf{u}}=-2\eta\frac{N_\delta}{p}\nabla\mathbf{u},\varepsilon=\frac{1}{\mathrm{Pr}(\gamma-1)}$$

In equation (8), the constant c is defined as $\left(mk_BT_{ref}\right)^{1/4}\Big/2d_{ref}\eta_{ref}^{1/2}$.

III. Numerical Methods to Solve the Conservation Laws and Constitutive Relations

A. Governing equation of conservation laws and temporal-spatial discretization

The three-dimensional dimensionless governing equations of conserved variables for a diatomic gas in conservative form in curvilinear coordinate system (τ,ξ,η,ζ) can be expressed as:

$$\frac{\partial\hat{\mathbf{Q}}}{\partial\tau}+\frac{\partial\hat{\mathbf{F}}_c}{\partial\xi}+\frac{\partial\hat{\mathbf{G}}_c}{\partial\eta}+\frac{\partial\hat{\mathbf{H}}_c}{\partial\zeta}+N_\delta\left(\frac{\partial\hat{\mathbf{F}}_v}{\partial\xi}+\frac{\partial\hat{\mathbf{G}}_v}{\partial\eta}+\frac{\partial\hat{\mathbf{H}}_v}{\partial\zeta}\right)=0, \tag{9}$$

where

$$\hat{\mathbf{Q}}=\frac{1}{J}\begin{bmatrix}\rho\\ \rho u\\ \rho v\\ \rho w\\ \rho E\end{bmatrix},\quad \hat{\mathbf{F}}_c=\frac{1}{J}\begin{bmatrix}\rho U\\ \rho uU+p\xi_x\\ \rho vU+p\xi_y\\ \rho wU+p\xi_z\\ (\rho E+p)U-p\xi_t\end{bmatrix},\quad \hat{\mathbf{G}}_c=\frac{1}{J}\begin{bmatrix}\rho V\\ \rho uV+p\eta_x\\ \rho vV+p\eta_y\\ \rho wV+p\eta_z\\ (\rho E+p)V-p\eta_t\end{bmatrix},$$

$$\hat{\mathbf{H}}_c=\frac{1}{J}\begin{bmatrix}\rho W\\ \rho uW+p\zeta_x\\ \rho vW+p\zeta_y\\ \rho wW+p\zeta_z\\ (\rho E+p)W-p\zeta_t\end{bmatrix},\hat{\mathbf{F}}_v=\frac{1}{J}\begin{bmatrix}0\\ \xi_x\left(\Pi_{xx}+\Delta\right)+\xi_y\Pi_{xy}+\xi_z\Pi_{xz}\\ \xi_x\Pi_{xy}+\xi_y\left(\Pi_{yy}+\Delta\right)+\xi_z\Pi_{yz}\\ \xi_x\Pi_{xz}+\xi_y\Pi_{yz}+\xi_z\left(\Pi_{zz}+\Delta\right)\\ \xi_xb_x+\xi_yb_y+\xi_zb_z\end{bmatrix},$$

$$\hat{\mathbf{G}}_v=\frac{1}{J}\begin{bmatrix}0\\ \eta_x\left(\Pi_{xx}+\Delta\right)+\eta_y\Pi_{xy}+\eta_z\Pi_{xz}\\ \eta_x\Pi_{xy}+\eta_y\left(\Pi_{yy}+\Delta\right)+\eta_z\Pi_{yz}\\ \eta_x\Pi_{xz}+\eta_y\Pi_{yz}+\eta_z\left(\Pi_{zz}+\Delta\right)\\ \eta_xb_x+\eta_yb_y+\eta_zb_z\end{bmatrix},\hat{\mathbf{H}}_v=\frac{1}{J}\begin{bmatrix}0\\ \zeta_x\left(\Pi_{xx}+\Delta\right)+\zeta_y\Pi_{xy}+\zeta_z\Pi_{xz}\\ \zeta_x\Pi_{xy}+\zeta_y\left(\Pi_{yy}+\Delta\right)+\zeta_z\Pi_{yz}\\ \zeta_x\Pi_{xz}+\zeta_y\Pi_{yz}+\zeta_z\left(\Pi_{zz}+\Delta\right)\\ \zeta_xb_x+\zeta_yb_y+\zeta_zb_z\end{bmatrix}. \tag{10}$$

In formulas (10), $\xi_x,\xi_y,\xi_z,\xi_t,\eta_x,\eta_y,\eta_z,\eta_t,\zeta_x,\zeta_y,\zeta_z,\zeta_t$ denote the metrics. ρ,u,v,w,E represent the density, the three coordinate components of velocity vector, and total energy per unit mass respectively. J is the Jacobian coordinate transformation and U,V,W are contravariant velocities, expressed as

$$\begin{aligned}U&=\xi_xu+\xi_yv+\xi_zw+\xi_t,\\ V&=\eta_xu+\eta_yv+\eta_zw+\eta_t,\\ W&=\zeta_xu+\zeta_yv+\zeta_zw+\zeta_t.\end{aligned}$$

and

$$\begin{aligned}b_x&=u\left(\Pi_{xx}+\Delta\right)+v\Pi_{xy}+w\Pi_{xz}+\varepsilon q_x,\\ b_y&=u\Pi_{yx}+v\left(\Pi_{yy}+\Delta\right)+w\Pi_{yz}+\varepsilon q_y,\\ b_z&=u\Pi_{zx}+v\Pi_{zy}+w\left(\Pi_{zz}+\Delta\right)+\varepsilon q_z.\end{aligned}$$

The linear Navier-Stokes-Fourier constitutive relations can be rewritten in an index form as (with the Stokes' hypothesis $\eta_b = 0$)

$$\begin{aligned}
&\Pi_{ij0} = -\eta\left(\frac{\partial u_j}{\partial x_i} + \frac{\partial u_i}{\partial x_j}\right) + \frac{2\eta}{3}\frac{\partial u_k}{\partial x_k}\delta_{ij}, \\
&\Delta_0 = -\eta_b \frac{\partial u_i}{\partial x_i} = 0, \\
&Q_{i0} = -\lambda\frac{\partial T}{\partial x_i}.
\end{aligned} \tag{11}$$

The linear constitutive relations (11) in conjunction with conservation laws (9) and (10) yield the well-known NS equations. In contrast, the dimensionless nonlinear coupled constitutive relations are written as

$$\begin{aligned}
&q\left(c\hat{R}\right)\hat{\Pi}_{ij} = \left(1+\hat{\Delta}\right)\hat{\Pi}_{ij0} + \frac{1}{2}\left(\hat{\Pi}_{ik}\frac{\partial \hat{u}_j}{\partial x_k} + \hat{\Pi}_{jk}\frac{\partial \hat{u}_i}{\partial x_k}\right) - \frac{1}{3}\hat{\Pi}_{mk}\frac{\partial \hat{u}_m}{\partial x_k}\delta_{ij}, \\
&q\left(c\hat{R}\right)\hat{\Delta} = \hat{\Delta}_0 + \frac{3}{2}f_b\left(\hat{\Pi}_{ij} + \hat{\Delta}\delta_{ij}\right)\frac{\partial \hat{u}_j}{\partial x_i}, \\
&q\left(c\hat{R}\right)\hat{Q}_i = \left(1+\hat{\Delta}\right)\hat{Q}_{i0} + \hat{\Pi}_{ij}\hat{Q}_{j0},
\end{aligned} \tag{12}$$

where $\hat{R}^2 = \hat{\Pi}_{ij}^2 + \left(2\gamma'/f_b\right)\hat{\Delta}^2 + \hat{Q}_i^2$. Together with conservation laws (9) and (10), the nonlinear relations (12) yield so-called NCCR equations.

The NCCR equations with the conservation laws in partial differential form and the constitutive relations in algebraic form, are attempted to be solved numerically within the finite volume framework. For computing the inviscid flux of hyperbolic conservational system, AUSMPW+ scheme was proposed by Kim [26] through introducing the pressure-based weight function to remove the oscillations of AUSM+ and overcome carbuncle phenomena of AUSMD. This flux splitting scheme is extensively used in hypersonic flows due to its efficiency, robustness and strong capability in capturing the shock. Therefore, the AUSMPW+ is also employed in computing the convective flux of NCCR equations. The AUSMPW+ scheme can be summarized as

$$F_{1/2} = c_{1/2}\left(\bar{M}_L^+\Phi_L + \bar{M}_R^-\Phi_R\right) + \left(P_L^+\Big|_{\alpha=3/16}\mathbf{P}_L + P_R^-\Big|_{\alpha=3/16}\mathbf{P}_R\right). \tag{13}$$

For the detail of each parameter in (13), see the literature [26]. Note that the magnitude of the viscosity is significant in simulating rarefied flows. High-resolution Van Albada limiter with less dissipation is utilized

together with Van Leer's MUSCL (Monotonic Upstream-Centred Scheme for Conservation Laws) approach to reconstruct the left and right values of the interface, which can be summarized as

$$\begin{aligned} q_{i+1/2}^{L} &= q_i + \frac{1}{4}\left[(1-k)\bar{\Delta}_- + (1+k)\bar{\Delta}_+\right]_i, \\ q_{i+1/2}^{R} &= q_{i+1} - \frac{1}{4}\left[(1-k)\bar{\Delta}_+ + (1+k)\bar{\Delta}_-\right]_{i+1}, \end{aligned} \tag{14}$$

where

$$\begin{aligned} &\bar{\Delta}_- = \bar{\Delta}_+ = Van\ albada\left(\Delta_-, \Delta_+\right), \\ &\left(\Delta_-\right)_i = q_i - q_{i-1},\ \left(\Delta_+\right)_i = q_{i+1} - q_i, \\ &Van\ albada\left(x, y\right) = \frac{x\left(y^2+\varepsilon\right) + y\left(x^2+\varepsilon\right)}{x^2 + y^2 + 2\varepsilon}. \end{aligned}$$

In above formula, ε is a small quantity in case of denominator's division by zero. The parameter k in (14) determines the spatial accuracy of the interpolation. For instance, $k=-1$ denotes a second-order upwind difference scheme while $k=1$ results in a purely central scheme. In this paper, $k=-1$ is adopted for capturing the discontinuous flows. The spatial derivatives of viscous flux are discretized by the second-order central difference scheme. For the temporal discretization, the implicit Lower-Upper Symmetric Gauss-Seidel (LU-SGS) scheme is adopted to get an efficient steady convergence. The governing equation (9) by the first-order implicit temporal discretization can be rewritten as

$$\left[\mathbf{I} + \Delta t\left(D_\xi \mathbf{A} + D_\eta \mathbf{B} + D_\zeta \mathbf{C}\right)\right]\Delta Q^n = -\Delta t \mathbf{RHS}, \tag{15}$$

where D_ξ, D_η, D_ζ are differential operators and $\mathbf{A}$, $\mathbf{B}$, $\mathbf{C}$ are inviscid Jacobian matrixes. $\mathbf{RHS}$ represents the residual. Finally, the LUSGS time-marching form can be derived by LU splitting as

$$\mathbf{L}\mathbf{D}^{-1}\mathbf{U}\Delta Q = -\mathbf{RHS}, \tag{16}$$

where

$$\begin{aligned} \mathbf{D} &= \mathbf{I}\left[\frac{1}{\Delta t} + \rho\left(\mathbf{A}\right) + \rho\left(\mathbf{B}\right) + \rho\left(\mathbf{C}\right)\right], \\ \mathbf{L} &= \mathbf{D} - \mathbf{A}_{i-1}^{+} - \mathbf{B}_{j-1}^{+} - \mathbf{C}_{k-1}^{+}, \\ \mathbf{U} &= \mathbf{D} + \mathbf{A}_{i+1}^{-} + \mathbf{B}_{j+1}^{-} + \mathbf{C}_{k+1}^{-}. \end{aligned}$$

Here $\mathbf{A}^{\pm}$, $\mathbf{B}^{\pm}$, $\mathbf{C}^{\pm}$ are approximate Jacobian matrixes and $\rho(\mathbf{A})$, $\rho(\mathbf{B})$, $\rho(\mathbf{C})$ are spectral radiuses for the inviscid Jacobian matrixes. In general, explicit temporal discretization of viscous term in (9) would lead to computational instability in viscosity-predominated region, such as boundary layer. In this work, we try to approximately discretize the viscous term in implicit way by utilizing the viscous spectral radiuses to modify the eigenvalues for approximate Jacobian matrixes. For instance, in case of ξ direction,

$$\bar{A}^{\pm} = A^{\pm} + k_A I \tag{17}$$

Note that the Jacobian matrixes for NCCR viscous terms are extremely complex to deduce the viscous spectral radiuses directly. The NSF's viscous spectral radiuses $k_A = 2Ma_{\infty}\mu\left|\nabla\xi\right|^2/\mathrm{Re}\,\rho$ are utilized for NCCR equations. Overall, the computational results show that this approximation meets the requirement of efficiency and stability for NCCR equations.

B. Undecomposed algorithm and an analysis on complicated algebraic constitutive relation

The only difference between NS and NCCR equations is the treatment of non-conserved variables appearing in conservation laws; viscous stresses and heat flux. They can be computed explicitly from the first-order derivative of conserved variable in NSF relations (11) but implicitly in NCCR model (12). The implicitness of $\hat{\Pi}_{ij}$, $\hat{\Delta}$, $\hat{Q}_i$ (output) for given thermodynamic forces (input) in NCCR model (12) is spawned by the presence of the exponential term, $q(\kappa) = \sinh(\kappa)/\kappa$. Therefore, an additional iterative process is required to numerically solve the NCCR model, which can be written as a general form of nonlinear implicit-type algebraic equations:

$$\begin{aligned}
f_1\left(\hat{\Pi}_{xx},\hat{\Pi}_{yy},\hat{\Pi}_{xy},\hat{\Pi}_{xz},\hat{\Pi}_{yz},\hat{Q}_x,\hat{Q}_y,\hat{Q}_z,\hat{\Delta}\right) &= 0,\\
f_2\left(\hat{\Pi}_{xx},\hat{\Pi}_{yy},\hat{\Pi}_{xy},\hat{\Pi}_{xz},\hat{\Pi}_{yz},\hat{Q}_x,\hat{Q}_y,\hat{Q}_z,\hat{\Delta}\right) &= 0,\\
&\vdots\\
f_9\left(\hat{\Pi}_{xx},\hat{\Pi}_{yy},\hat{\Pi}_{xy},\hat{\Pi}_{xz},\hat{\Pi}_{yz},\hat{Q}_x,\hat{Q}_y,\hat{Q}_z,\hat{\Delta}\right) &= 0,
\end{aligned} \tag{18}$$

where f_i can be defined as a function of nine independent variables $\left(\hat{\Pi}_{xx},\hat{\Pi}_{yy},\hat{\Pi}_{xy},\hat{\Pi}_{xz},\hat{\Pi}_{yz},\hat{Q}_x,\hat{Q}_y,\hat{Q}_z,\hat{\Delta}\right)$, mapping a 9-dimensional space $\mathbb{R}^9$ into the real line $\mathbb{R}$. A more compact vector form of the nonlinear equation systems (18) can be rewritten as:

$$\mathbf{F}(\mathbf{x})=0, \tag{19}$$

where $\mathbf{F}=\left(f_1, f_2,\ldots, f_9\right)^t$ and $\mathbf{x}=\left(\hat{\Pi}_{xx},\hat{\Pi}_{yy},\hat{\Pi}_{xy},\hat{\Pi}_{xz},\hat{\Pi}_{yz},\hat{Q}_x,\hat{Q}_y,\hat{Q}_z,\hat{\Delta}\right)^t$.

Owing to the highly nonlinear terms in (18), Myong proposed a decomposed algorithm [15, 17, 27] based on the concept of the splitting of the flow into two distinct components, as shown in Figure 1. The decomposed algorithm was adopted to solve a decomposed nonlinear algebraic system [28] rather than directly solve the complete system (18) of NCCR model. That is, in the case of a three-dimensional problem, the stress tensor and heat flux vector components $\left(\Pi_{xx},\Pi_{xy},\Pi_{xz},\Delta,Q_x\right)$ on a surface in the three-dimensional finite volume induced by thermodynamics forces $\left(u_x,v_x,w_x,T_x\right)$ can be approximated as the sum of two decomposed solvers: one on $\left(u_x,0,0,T_x\right)$ describing the compression and expansion flows, and another on $\left(0,v_x,0,0\right)$ and $\left(0,0,w_x,0\right)$ describing shear flows.

In our recent undecomposed work, two numerical approximation methods, the fixed-point iteration $\mathbf{x}=G(\mathbf{x})$ and Newton's method $\mathbf{G}(\mathbf{x})=\mathbf{x}-J(\mathbf{x})^{-1}\mathbf{F}(\mathbf{x})$, are considered for solving aforementioned complete systems of nonlinear algebraic equations (19). In fixed-point iteration, the first challenge is to construct an available convergent iterative expression for the NCCR model. The evolution equations (12) for NCCR's non-conserved variables (shear stress, bulk stresses and heat flux) can be rewritten in a simple form $q\left(c\hat{R}\right)\hat{R}^2=F$, recalling the Rayleigh-Onsager dissipation function, in the sense that it conserves the whole information of non-conserved variables by one scalar formulation

$$F=\hat{\Pi}_{ij}\left[\left(1+\hat{\Delta}\right)\hat{\Pi}_{ij0}+\frac{1}{2}\left(\hat{\Pi}_{ik}\frac{\partial\hat{u}_j}{\partial x_k}+\hat{\Pi}_{jk}\frac{\partial\hat{u}_i}{\partial x_k}\right)-\frac{1}{3}\hat{\Pi}_{mk}\frac{\partial\hat{u}_m}{\partial x_k}\delta_{ij}\right]$$
$$+\left(2\gamma'/f_b\right)\hat{\Delta}\left[\hat{\Delta}_0+\frac{3}{2}f_b\left(\hat{\Pi}_{ij}+\hat{\Delta}\delta_{ij}\right)\frac{\partial\hat{u}_j}{\partial x_i}\right]+\left[\left(1+\hat{\Delta}\right)\hat{Q}_{i0}+\hat{\Pi}_{ij}\hat{Q}_{j0}\right]\hat{Q}_i,$$

and improves the computation efficiency by reducing the amount of iterative scalar equations. $\hat{R}$ serves as an intermediate variable in the iteration $\hat{R}_{n+1} = \sinh^{-1}\left(cF_n / \hat{R}_n\right)/c$. The fixed-point iterative formulation is stable, but can merely cover most domains rather than the whole range in $\hat{u}_x$-only and $\hat{v}_x$-only testing problems.

On the other hand, the Newton's method—although it is generally expected to have quadratic convergence—is extremely sensitive to the starting value and invertibility of matrix $J\left(\mathbf{x}\right)^{-1}$. Owing to NCCR model's complex mathematical properties and subject to single method's iterative limitation, it is hard to obtain convergence for all flow regimes incorporating a wide range of thermodynamic forces (local gradients of flow parameters) by a single method. But, interestingly, it was found that the combination of these two iterative methods' convergent regions could cover the whole range of thermodynamic forces for the NCCR model. Therefore, an undecomposed hybrid algorithm with combination of fixed-point and Newton's iterations is proposed for completely solving the NCCR model on the basis of their convergent conditions. In our hybrid solver, we switch to use one of the two iterative methods in the computation of the flow region when the other one fails to yield convergent solution.

The distinction between the decomposed and the undecomposed algorithm is from their solution systems (reduced or complete) of NCCR model and the specific solution methods (splitting or non-splitting). In order to compare our undecomposed solution and Myong's previous decomposed works [14, 15, 17], the nonlinear constitutive curves of diatomic gases in one-dimensional compression-expansion ($\hat{u}_x$-only) and shear ($\hat{v}_x$-only) problems are analysed. In these two simple flow problems, we try to demonstrate the variation of each stress component with the derivative of velocities $\hat{u}$ and $\hat{v}$ in *x*-coordinate direction. Figure 2 shows variations of components of the normal stress $\hat{\Pi}_{xx}$, $\hat{\Pi}_{yy}$, $\hat{\Pi}_{zz}$ and the excess normal stress $\hat{\Delta}$ with $\hat{u}_x$, while Figure 3 demonstrates their relations with $\hat{v}_x$. Note that the normal stresses $\hat{\Pi}_{yy}$ and $\hat{\Pi}_{zz}$ cannot be computed directly in two solvers (one for $\hat{u}_x$-only and another for $\hat{v}_x$-only problems) of the decomposed algorithm. Therefore, the

decomposed solutions of $\hat{\Pi}_{yy}$ and $\hat{\Pi}_{zz}$ originate from two simple relations, $\hat{\Pi}_{yy}=\hat{\Pi}_{zz}=-\hat{\Pi}_{xx}/2$ for $\hat{u}_x$–only and $\hat{\Pi}_{xx}=\hat{\Pi}_{zz}=-\hat{\Pi}_{yy}/2$ for $\hat{v}_x$-only. To some extent, $\hat{u}_x$ and $\hat{v}_x$ can be regarded as the level of departure from the local equilibrium state. All the figures for the NCCR model demonstrate strong nonlinearity in comparison with the linear NSF constitutive relations. The NCCR model yields very different asymptotic behaver when $\hat{u}_x,\hat{v}_x\to\infty,-\infty$, but recovers smoothly to the linear NSF solutions in the local equilibrium $\hat{u}_x=\hat{v}_x=0$, which implies inclusive of the conventional NSF model. Furthermore, it can be seen that undecomposed solutions yield excellent agreement with decomposed solutions of normal stresses $\hat{\Pi}_{xx}$, $\hat{\Pi}_{yy}$, $\hat{\Pi}_{zz}$, shear stress $\hat{\Pi}_{xy}$ and excess normal stress $\hat{\Delta}$.

In order to evaluate the improvement of the undecomposed method in solving the NCCR model in comparison with the decomposed method, a (ideal) combined compression-expansion-shear flow is considered for examining the $\hat{u}_x$– and $\hat{v}_x$ –induced undecomposed effects. (Note that in real compressible flow problems non-zero $\hat{u}_x$ will always be accompanied by non-zero $\hat{T}_x$.) Figure 4 demonstrates the difference between the undecomposed and decomposed solutions of $\hat{\Pi}_{xx}$, $\hat{\Pi}_{xy}$, $\hat{\Delta}$ in the $\hat{u}_x$ - $\hat{v}_x$ -only problem. The undecomposed algorithm computes the non-conserve variables strictly under the complete mathematical constraint of the nonlinear constitutive model (NCCR). On the other hand, the decomposed algorithm splits the fully coupled problems into several non-interfering subset cases. By doing so, it can achieve better computational convergence in these one-dimensional numerical issues, since the mathematical well-posedness and numerical convergence of subset cases can be easily proven.

In the treatment of a three-dimensional problem in case of decomposed algorithm, the stress and heat flux components $\left(\hat{\Pi}_{xx},\hat{\Pi}_{xy},\hat{\Pi}_{xz},\hat{\Delta},\hat{Q}_x\right)$ on a plane in the three-dimensional physical control volume induced by thermodynamic forces $\left(\hat{u}_x,\hat{v}_x,\hat{w}_x,\hat{T}_x\right)$ are computed by a linear summation of two subset solvers: (1) one on $\left(\hat{u}_x,0,0,\hat{T}_x\right)$, and (2) another on $\left(0,\hat{v}_x,0,0\right)$ or $\left(0,0,\hat{w}_x,0\right)$. Therefore, in the ideal $\hat{u}_x$ - $\hat{v}_x$ -only problem, the

decomposed solution process, by definition, will neglect the interplay effect induced simultaneously by $\hat{u}_x$ and $\hat{v}_x$, as shown in Figure 5 of the stress $\hat{\Pi}_{yy}$ and $\hat{\Pi}_{zz}$. Furthermore, a three-dimensional compression-expansion problem ($\hat{u}_x$ - $\hat{v}_y$ - $\hat{w}_z$ -only) are also computed to evaluate the differences between the undecomposed and decomposed solutions, which are summarized in Figure 6. It remains, however, to be seen that these differences arose from the interplay effect of velocity gradients will produce a meaningful impact on the final solutions of flow field, which are determined not only by the constitutive relations but also by conservation laws.

Finally, the computational cost of two algorithms for $\hat{u}_x$ -only, $\hat{v}_x$ -only and $\hat{u}_x$ - $\hat{v}_x$ -only problems with non-equilibrium level is shown in Figure 7. The number of iteration in the vertical axis denotes the extra computational consumption in calculation of viscous flux term at every time-marching step and the horizontal axis represents the level of departure from equilibrium. Note that linear NSF stress and heat flux are computed explicitly from $\left(\hat{u}_x, \hat{v}_x, \hat{w}_x, \hat{T}_x\right)$. The computational cost for NSF solver can be assumed to be unity as a criterion for NCCR solvers. As is depicted in Figure 7, the computation cost of present undecomposed algorithm is generally lower than that of decomposed algorithm, except for the $\hat{v}_x$ -only problem at far-from-equilibrium regime.

IV. Results and Discussion

The nonlinear constitutive model of diatomic gases has been successfully applied to the computation of shock wave structure [22, 24, 25], micro-Couette flow [29], etc. In this paper, the model is further extended to stable and efficient computation of high-speed flows past three-dimensional flying configurations, in particular, within finite volume framework, by utilizing a new undecomposed hybrid algorithm on the constitutive equations.

A. Hypersonic flow past a blunted cone tip

The first case studied is a 25^0 half angle cone with a blunted nose of 6.35 mm in radius. Since the wake

region behind the cone is not of main interest, the configuration is assumed to be infinitely long but be truncated to have its first 5 cm length from the leading edge. Note that there is no angle attack in this flow and the cone tip is axisymmetric. Structured grid of 0.58 million is used in all computations, as shown in Figure 8. The working gas is assumed to be pure nitrogen and the free-stream conditions are chosen from the Run 31 of CUBRC experiments [30] with $U_\infty = 2764.5 m/s$, $T_\infty = 144.4K$, $p_\infty = 21.907 Pa$, $Ma_\infty = 11.3$. An isothermal temperature condition with T_w=297.2K and an accommodation coefficient of unity at the wall are assumed. The gas viscosity is computed by using the inverse power laws

$$\eta = \eta_{ref} \left(\frac{T}{T_{ref}} \right)^s . \tag{20}$$

Other physical properties of nitrogen used in computations are summarized in Table 1

Figure 9-11 respectively demonstrate the DSMC, NSF and NCCR solutions of velocity and density along the lines normal to the cone at stagnation point, *X*= 1.14 and *X*= 3.14 cm. The DSMC data used in comparison are obtained from Boyd's code (MONACO) and more details on the DSMC computation are described in [31]. The flow along the stagnation line passing through a normal shock wave is strongly non-equilibrium and the linear NSF and DSMC solutions are therefore expected to be different to a large extent. In fact, as depicted in Figure 9, the NSF results are significantly different from the DSMC results for the shock thickness and strength in local region of cone tip. On the other hand, the NCCR results yield excellent agreement with the DSMC results.

Similar comparisons between DSMC and NCCR solutions are shown for velocity and density at *X*= 1.14 and *X*= 3.14 cm in Figure 10-11. At these locations, the effect of non-equilibrium of oblique shock wave is not as strong as that of the stagnation line, and consequently the NSF model with a slip boundary performs reasonably well. As shown in the figures, both NSF and NCCR results are very close to the DSMC results in most regions, except for NSF solutions in the oblique shock region. The discrepancies of NSF in velocity profiles are also

highlighted in Figure 10-11(a). In general, the NCCR model performs better than the NSF model in predicting nonequilibrium flows.

B. Complex flow past a hollow cylinder-flare

To further validate the present computational model before applying to the complex flow problem of real vehicles in near-space regime, we consider a complex flow past a hollow cylinder-flare. In this case, the data of winds tunnel experiments made in the CUBRC LENS facility [32] are available. The case has also been extensively studied in literatures [31, 33, 34] containing a large amount of DSMC and NS data.

The configuration of a hollow cylinder in conjunction with a 30^o conical flare is depicted in Figure 12. It is worthwhile mentioning that the sharp leading edge separates the free-stream and only the external flow of the configuration is taken into account in the calculation, since the internal flow does not interact with the external flow. The working gas is assumed pure nitrogen. The inputs including the free-stream conditions are listed as

$$\begin{aligned} &L = 0.1017m && \mathrm{U}_\infty = 2301.7m/s \\ &T_\infty = 118.2K && \rho_\infty = 9.023\times10^{-4} kg/m^3 \\ &T_w = 295.6K && R = 296m^2/\left(\sec^2\cdot K\right) \\ &Kn_\infty = 6.5\times10^{-4} && Ma_\infty = 10.4 \\ &\eta_{ref} = 1.656\times10^{-5}\ \mathrm{N}\cdot s/m^2 && T_{ref} = 273K \end{aligned} \tag{21}$$

Notice that the free-stream condition is non-equilibrium in CUBRC Run 14 as the translational, rotational and vibrational temperatures are at different time scales. However, since the NCCR model at present does not include vibrational non-equilibrium effects, no vibrational energy exchange for a diatomic gas is considered in our simulation. According to Myong [15], the excess normal stress associated with the bulk viscosity of a diatomic gas could be introduced to describe the rotational non-equilibrium effect in some flow regimes where the rotational relaxation is faster than the hydrodynamic scale. Here we focus mainly on in what range of flow regime the NCCR model without this additional physical effect can handle the high-temperature high-speed

flows.

From the gradient-length-local Knudsen contours in Figure 13, continuum breakdown occurs inside oblique shock wave above the flare and the region between sharp leading edge and the separation region. The separation and re-attachment region can be observed clearly in Figure 14. The Mach number contour predicted by NCCR model demonstrates its capability of simulating this hypersonic flow fairly well. Since the separation point is x/L=0.5, flow fields along the lines normal to the cylinder body at x/L=0.5 and 1 are studied in detail. Figure 15 shows the comparisons for density and velocity properties of DSMC, NSF and NCCR along these two lines. Notice that there is no comparison for temperature in this study now that the present NCCR model has not taken the vibrational non-equilibrium effect into account. The DSMC and NSF results from the literature [31] and the DSMC results computed by a parallel optimized code named MONACO are used for comparison. As shown in the left of Figure 15, the NCCR results are in better agreement with the DSMC results than NSF results along the line normal to the cylinder at x/L=0.5, which is considered to be far removed from local thermodynamic equilibrium based on continuum breakdown parameter Kn_{GLL}. In the right profiles of Figure 15, the NCCR results are only in qualitative agreement with DSMC results, but capture excellently a small discontinuity around the shock region which is not captured by NSF. Boyd et al.[31] pointed out that the DSMC provides correct solution before the separation point, but the accuracy at the conjunction of the cylinder and flare(x/L=1) is questionable. The deviation between NCCR and DSMC results makes it difficult to judge the performance and a further study is needed to clarify this issue.

In Figure 16, numerical results are compared with the experimental data for non-dimensionless heat flux coefficient, defined as $C_q = q_w / 0.5\rho_\infty U_\infty^3$, along the body surface. The NCCR solutions are found to be in excellent agreement with the experimental data, especially in the separation and re-attachment points (about x/L=0.6 and 1.4). On the other hand, the DSMC over-predicts the size of the separation and re-attachment region,

while the NSF and under-predicts it.

C. Slip flow past a HTV-type vehicle

Lastly, the hypersonic rarefied flows around 3D real flying configuration in near-equilibrium or far-from-equilibrium flow regime are investigated to evaluate the performance of the NCCR model. High-speed flow fields (Mach number 25 and 20) past a lifting body (a HTV-type vehicle) at the altitude of 50 and 90 kilometres are computed. Figure 17 shows the basic configuration of the HTV-type vehicle. Two angles of attack (20^0 and 0^0) are considered. Isothermal walls with a constant wall temperature 1000K are assumed. The viscosity of air is computed by the inverse power laws (20) and the other properties of air used in computations are given in Table 2.

The Maxwell-Smoluchowski slip boundary conditions with full tangential momentum and thermal accommodation coefficients are employed at the solid surface. The linear NSF with slip conditions is known to be capable of simulating this flow regime around the 2-meters-long HTV-type vehicle at altitudes of 50 and 90 kilometres, which may be defined as continuum and slip flow regimes, respectively, according to the body-length global (BLG) Knudsen number [35]

$$Kn_{BLG} = \frac{l_\infty}{L}. \tag{22}$$

Here l_∞ is the free-stream mean free path and L is the characteristic body length.

However, a non-negligible local rarefaction effect can be found especially in sharp leading edge, shock wave region or wake leeward region of hypersonic vehicles, which are far from local-equilibrium and out of the capability of NSF model based on near-local-equilibrium. Therefore, we adopt the second-order nonlinear model (NCCR) to simulate these flows, in hope of achieving a significant improvement in two aspects: recovering the NSF solution in continuum regime and remedying for the NSF solution in continuum breakdown regions.

Firstly, a grid independence study is carried out for the NCCR model with three sets of grids. The detailed information of these grids is given in Table 3. Refined grids 2 and 3 yield almost the same solution, while coarse grid 1 shows obvious deviation in Mach profile, as illustrated in Figure 18. By taking efficiency into consideration, we selected refined grid 2 for further investigation.

Next, as a step toward evaluating the potential of the second-order NCCR model in engineering application, non-equilibrium regions of sharp leading edge, as well as surface aerothermal and aerodynamic properties including pressure, friction and heating transfer rate of the vehicle, are investigated. The pressure, skin friction coefficient and heat transfer rate in Figure 26-27 are defined, respectively, as

$$C_p = \frac{p - p_\infty}{0.5\rho_\infty U_\infty^2}, \quad C_f = \frac{\tau}{0.5\rho_\infty U_\infty^2}, \quad C_h = \frac{q}{0.5\rho_\infty U_\infty^3}. \tag{23}$$

Figure 19 shows the details of pressure contour and streamline pattern around the sharp leading edge on symmetrical plane, from which a strong shock wave structure and a weak re-attachment region can be observed clearly. In order to compare the locations of the shock wave structure around the edge predicted by NSF and NCCR model, macro-variable distributions from three important positions ($X = 0.1Rb$, $X = 0.5Rb$, $X = 1.0Rb$) along the y direction on the symmetrical plane are examined. As shown in Figure 20, both NSF and NCCR can capture the steep shock structure accurately and its location is predicted exactly the same, which implies that the NCCR model shows excellent performance in continuum regime as the linear NSF model does.

Figure 21 yields distribution profiles of another case at 90 kilometres high. It is worth mentioning that some significant discrepancies occur in these profiles between the near-local-equilibrium NSF results and the far-from-equilibrium NCCR results; e.g., the pressure values predicted by NSF are much higher than that by NCCR. In addition, it can be seen from pressure fields of Figure 22 that the shock wave becomes weaker in comparison with that of Figure 19, due to the lower density at 90 kilometres. That is, rarefaction effect becomes important and accounts for the substantial discrepancies in these profiles. A global impression and a local

impression of the Mach solutions by NSF and NCCR model are given for these two cases in Figure 23 and Figure 24 respectively. The flow structures remain almost the same at 50 km but demonstrate slight difference at 90 km, from which there exists a weaker solution of shock wave structure by NCCR than by NSF. As is also shown in Figure 24, the shock layer predicted by NCCR is thicker than that by NSF at 90km while their solutions of the flow distribution are the same in the shock layer at 50km, implying a strong rarefaction effect at 90km and a week one at 50km for this vehicle configuration.

Finally, Figure 25 shows the comparison of the after-body flows at different altitudes predicted by NS and NCCR. NCCR solution of after-body flow is consistent with NSF at 50 km, while the rarefied non-equilibrium effect at 90 km starts to kick in and causes significant discrepancy between two models. Moreover, non-negligible differences in the profiles of surface property between NS and NCCR model are also found. A slight difference is shown in skin friction and heat transfer coefficient profiles in Figure 26. The pressure, skin friction coefficients and heat transfer rate predicted by NCCR are much lower than those by NSF in Figure 27. NSF may overestimate the aerodynamic and aerothermal properties in rarefied hypersonic flows with a strong non-equilibrium effect.

V. Conclusions

The present study focuses on the development of computational NCCR model of diatomic gases for three-dimensional flows in rarefied hypersonic applications within finite volume framework. A new hybrid algorithm, which takes advantage of two conventional iterative methods—fixed-point and Newton's iterations, is developed for efficient computation of NCCR model. Also, modification of the iterative numerical method from decomposed to undecomposed in the present finite volume framework was found to enhance the numerical stability, in particular, for three-dimensional complicated flow problems.

Numerical experiments have been carried out on three-dimensional flow cases, including pure nitrogen gas flow past a blunted cone tip, complex flow past the hollow cylinder-flare, and slip flows past a HTV-type lifting-body flying configuration at 50 and 90 kilometres. Overall, the NCCR model can recover the NSF solution in continuum regime and yields better agreement with the DSMC and experiment data than NSF in local non-equilibrium regions. We also found that the discrepancies of flow field and surface properties between NSF and NCCR solutions increase as the flow becomes more rarefied in high-speed regime. On the whole, it can be concluded from the study of three rarefied hypersonic flows that the NCCR model is as computationally efficient as the NSF model in continuum regime, and, at the same time, more accurate in comparison with DSMC and experimental data than NSF in non-equilibrium flows.

VI. Acknowledgements

This research was funded by the National Natural Science Foundation of China (Grant NO. 11502232, 51575487, 11572284, and 61627901), the National Basic Research Program of China (Grant NO. 2014CB340201). The first author of this paper (Zhongzheng Jiang) gratefully acknowledges the support by the China Scholarship Council (grant number 201706320214). Furthermore, he would also like to thank Prof. Dr. Manuel Torrilhon and his group for their hospitality, and Mathematics Division in the Center for Computational Engineering Science at RWTH Aachen University for the available resources during his stay as joint-training Ph.D. student. R. S. Myong acknowledges the support from the National Research Foundation of Korea funded by the Ministry of Science and ICT (NRF 2017-R1A2B2007634), South Korea.

VII. References

1. Bird, G. A. *Molecular gas dynamics and the direct simulation of gas flows*. Oxford: Clarendom Press, 1994.

2. Grad, H. "Asymptotic theory of the Boltzmann equation," *Physics of Fluids* Vol. 6, No. 2, 1963, pp. 147-181. https://doi.org/10.1063/1.1706716

3. Bhatnagar, P. L., Gross, E. P., and Krook, M. "A model for collision processes in gases. I. Small amplitude processes in charged and neutral one-component systems," *Physical Review* Vol. 94, No. 3, 1954, pp. 511-525. https://doi.org/10.1103/PhysRev.94.511

4. Holway, L. H. "New statistical models for kinetic theory: methods of construction," *The Physics of Fluids* Vol. 9, No. 9, 1966, pp. 1658-1673. https://doi.org/10.1063/1.1761920

5. Shakhov, E. M. "Generalization of the Krook kinetic relaxation equation," *Fluid Dynamics* Vol. 3, No. 5, 1968, pp. 95-96. https://doi.org/10.1007/BF01029546

6. Broadwell, J. E. "Study of rarefied shear flow by the discrete velocity method," *Journal of Fluid Mechanics* Vol. 19, No. 03, 2006, p. 401. https://doi.org/10.1017/S0022112064000817

7. Xu, K., and Huang, J.-C. "A unified gas-kinetic scheme for continuum and rarefied flows," *Journal of Computational Physics* Vol. 229, No. 20, 2010, pp. 7747-7764.https://doi.org/10.1016/j.jcp.2010.06.032

8. Burnett, D. "The Distribution of Molecular Velocities and the Mean Motion in a Non-Uniform Gas," *Proceedings of the London Mathematical Society* Vol. s2-40, No. 1, 1936, pp. 382-435. https://doi.org/10.1112/plms/s2-40.1.382

9. Zhong, X., Maccormack, R. W., and Chapman, D. R. "Stabilization of the Burnett equations and application to hypersonicflows," *AIAA Journal* Vol. 31, No. 6, 1993, pp. 1036-1043. https://doi.org/10.2514/3.11726

10. Zhao, W., Chen, W., and Agarwal, R. K. "Formulation of a new set of Simplified Conventional Burnett equations for computation of rarefied hypersonic flows," *Aerospace Science and Technology* Vol. 38, 2014, pp. 64-75. http://dx.doi.org/10.1016/j.ast.2014.07.014

11. Grad, H. "On the kinetic theory of rarefied gases," *Comm.Pure Appl. Math* Vol. 2, 1949, pp. 331-407. https://doi.org/10.1002/cpa.3160020403

12. Torrilhon, M. "Modeling nonequilibrium gas flow based on moment equations," *Annual Review of Fluid Mechanics* Vol. 48, No. 1, 2016, pp. 429-458. https://doi.org/10.1146/annurev-fluid-122414-034259

13. Eu, B. C. *Kinetic theory and irreversible thermodynamics*. New York: Wiley, 1992.

14. Myong, R. S. "Thermodynamically consistent hydrodynamics computational models for high-Knudsen-number gas flows," *Physics of Fluids* Vol. 11, No. 9, 1999, pp. 2788-2802. https://doi.org/10.1063/1.870137

15. Myong, R. S. "A generalized hydrodynamic computational model for rarefied and microscale diatomic gas flows," *Journal of Computational Physics* Vol. 195, No. 2, 2004, pp. 655-676. https://doi.org/10.1016/j.jcp.2003.10.015

16. Rana, A., Ravichandran, R., Park, J. H., and Myong, R. S. "Microscopic molecular dynamics characterization of the second-order non-Navier-Fourier constitutive laws in the Poiseuille gas flow," *Physics of Fluids* Vol. 28, No. 8, 2016, p. 082003. https://doi.org/10.1063/1.4959202

17. Myong, R. S. "A computational method for Eu's Generalized Hydrodynamic Equations of rarefied and microscale gasdynamics," *Journal of Computational Physics* Vol. 168, No. 1, 2001, pp. 47-72. https://doi.org/10.1006/jcph.2000.6678

18. Jiang, Z., Zhao, W., and Chen, W. "A three-dimensional finite volume method for conservation laws in conjunction with modified solution for nonlinear coupled constitutive relations," *the 30th International Symposium on Rarefied Gas Dynamics*. Vol. 1786, American Institute of Physics, Victoria, British Columbia, Canada, 2016, p. 040002. https://doi.org/10.1063/1.4967540

19. Jiang, Z., Chen, W., and Zhao, W. "Numerical simulation of three-dimensional high-speed flows using a second-order nonlinear model," *21st AIAA International Space Planes and Hypersonics Technologies Conference*. American Institute of Aeronautics and Astronautics, Xiamen, China, 2017.

20. Eu, B. C. *Generalized thermodynamics: The thermodynamics of irreversible processes and generalized hydrodynamics*. New York: Kluwer Academic Publishers, 2002.

21. Al-Ghoul, M., and Eu, B. C. "Generalized hydrodynamics and shock waves," *Physical Review E* Vol. 56, 1997, pp. 2981-2992. https://doi.org/10.1103/PhysRevE.56.2981

22. Eu, B. C., and Ohr, Y. G. "Generalized hydrodynamics, bulk viscosity, and sound wave absorption and dispersion in dilute rigid molecular gases," *Physics of Fluids* Vol. 13, No. 3, 2001, pp. 744-753. https://doi.org/10.1063/1.1343908

23. Myong, R. S. "On the high Mach number shock structure singularity caused by overreach of Maxwellian molecules," *Physics of Fluids* Vol. 26, No. 5, 2014, p. 056102. https://doi.org/10.1063/1.4875587

24. Zhao, W., Jiang, Z., and Chen, W. "Computation of 1-D shock structure using nonlinear coupled constitutive relations and generalized hydrodynamic equations," *the 30th International Symposium on Rarefied Gas Dynamics*. Vol. 1786, American Institute of Physics, Victoria, British Columbia, Canada, 2016, p. 140007. https://doi.org/10.1063/1.4967638

25. Jiang, Z., Zhao, W., Chen, W., and Agarwal, R. K. "Computation of shock wave structure using a simpler set of generalized hydrodynamic equations based on nonlinear coupled constitutive relations," *Shock Waves*, 2019. https://doi.org/10.1007/s00193-018-0876-3

26. Kim, K. H., Kim, C., and Rho, O.-H. "Methods for the accurate computations of hypersonic flows: I. AUSMPW+ scheme," *Journal of Computational Physics* Vol. 174, No. 1, 2001, pp. 38-80.

https://doi.org/10.1006/jcph.2001.6873

27. Myong, R. S. "Impact of computational physics on multi-scale CFD and related numerical algorithms," *Computers & Fluids* Vol. 45, No. 1, 2011, pp. 64-69. https://doi.org/10.1016/j.compfluid.2011.01.011

28. Jiang, Z., Chen, W., and Zhao, W. "A new coupled computational method in conjunction with three-dimensional finite volume schemes for nonlinear coupled constitutive relations," *arXiv preprint arXiv:1611.01281*, 2016.

29. Jiang, Z., Chen, W., and Zhao, W. "Numerical analysis of the micro-Couette flow using a non-Newton–Fourier model with enhanced wall boundary conditions," *Microfluidics and Nanofluidics* Vol. 22, No. 1, 2017, p. 10. https://doi.org/10.1007/s10404-017-2028-y

30. Holden, M. "Experimental database from CUBRC studies in hypersonic laminar and turbulent interacting flows including flowfield chemistry," *Prepared for RTO code validation of DSMC and Navier-Stokes code validation studies, Calspan-University at Buffalo Research Center, Buffalo, NY*, 2000, pp. 105-114.

31. Wang, W.-L., and Boyd, I. D. "Hybrid DSMC-CFD Simulations of Hypersonic Flow over Sharp and Blunted Bodies," *36th AIAA Thermophysics Conference*. Orlando, Florida, 2003, pp. 1-13.

32. Holden, M. S. "Measurement in regions of laminar shock wave/boundary layer interaction in hypersonic flow-code validation." CUBRC Report, 2003.

33. Harvey, J. K. "A Review of a Validation Exercise on the use of the DSMC Method to Compute Viscous/Inviscid Interactions in Hypersonic Flow," *36th AIAA Thermophysics Conference*. Orlando, Florida, 2003.

34. Jiang, T., Xia, C., and Chen, W. "An improved hybrid particle scheme for hypersonic rarefied-continuum flow," *Vacuum* Vol. 124, 2016, pp. 76-84. https://doi.org/10.1016/j.vacuum.2015.11.

012

35. Boyd, I. D., Graham, G. C., and Candler, V. "Predicting failure of the continuum fluid equations in transitional hypersonic flows," *Physics of Fluids* Vol. 7, No. 1, 1995, pp. 210-219. https://doi.org/10.1063/1.868720

36. Ioannis K., and Nikolos, A. K. "Modeling of rarefied hypersonic flows using the massively parallel DSMC kernel"SPARTA"," *8th GRACM International Congress on Computational Mechanics*. Volos, 2015.

.

Table 1. Physical gas properties of pure nitrogen gas

γ	Pr	R(J/kg·K)	c	f_b	T_{ref} (K)	η_{ref} (Pa·s)	s_{VHS}
1.4	0.72	296.7	1.02029	0.8	273	1.656×10^{-5}	0.74

Table 2. Physical gas properties of air

γ	Pr	R(J/kg·K)	c	f_b	T_{ref} (K)	η_{ref} (Pa·s)	s_{VHS}
1.4	0.72	287.1	1.01445	0.8	273.15	1.71608×10^{-5}	0.77

Table 3. Grid independence study

	Grid points in normal, flow and circumferential directions	Grid spacing nearest to the solid wall
Mesh 1	$60\times120\times140$	5×10^{-5}
Mesh 2	$130\times150\times160$	5×10^{-5}
Mesh 3	$180\times170\times200$	1×10^{-5}

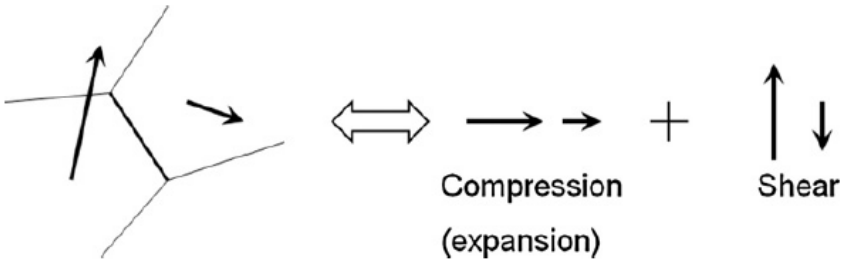

Figure 1. Splitting of the flow into two distinct components (compression-expansion and shear flows) [27]

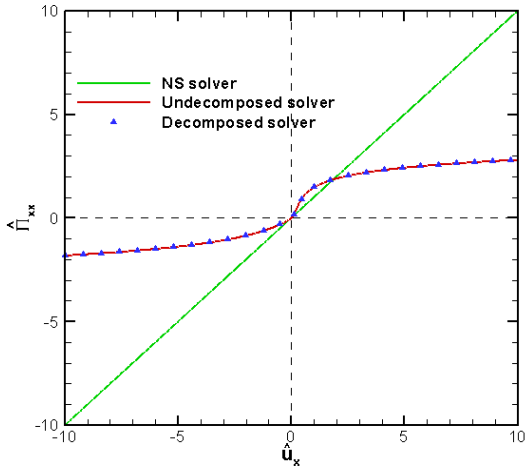

(a) Variation of $\hat{\Pi}_{xx}$ with $\hat{u}_x$

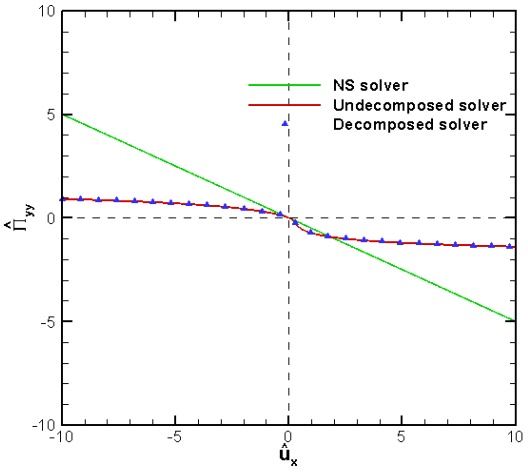

(b) Variation of $\hat{\Pi}_{yy}$ with $\hat{u}_x$

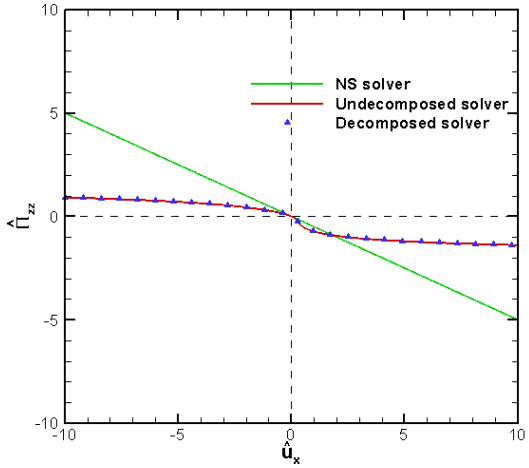

(c) Variation of $\hat{\Pi}_{zz}$ with $\hat{u}_x$

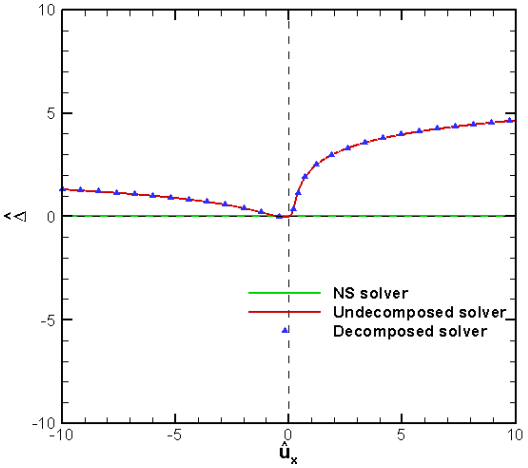

(d) Variation of $\hat{\Delta}$ with $\hat{u}_x$

Figure 2. Constitutive relations in the $\hat{u}_x$ -only problem for a diatomic gas

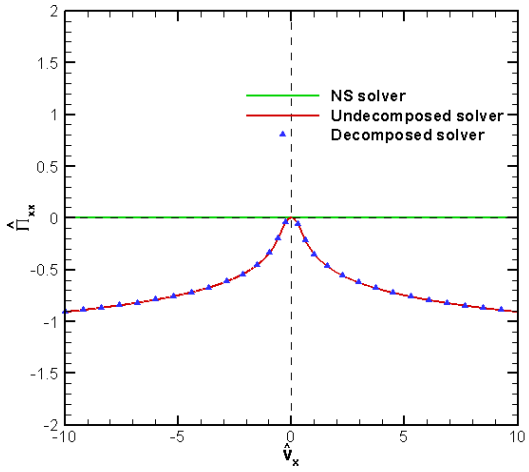

(a) Variation of $\hat{\Pi}_{xx}$ with $\hat{v}_x$

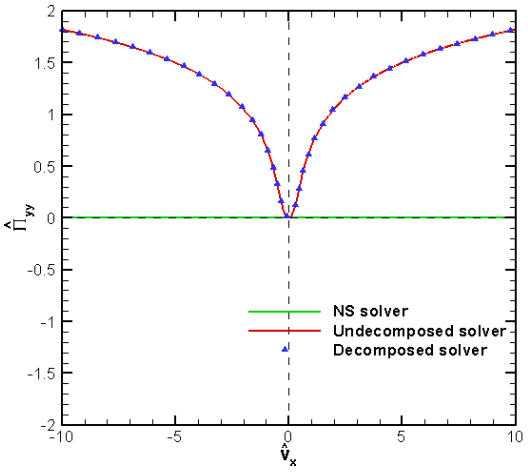

(b) Variation of $\hat{\Pi}_{yy}$ with $\hat{v}_x$

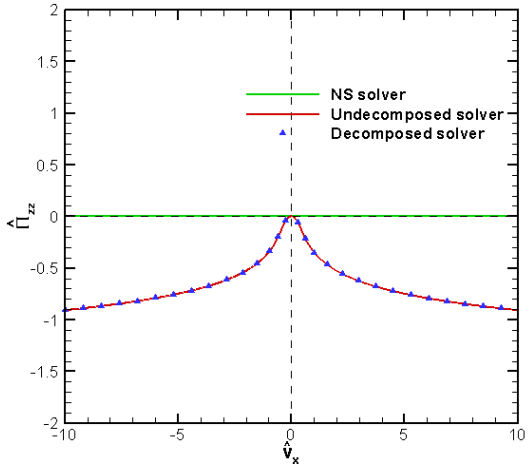

(c) Variation of $\hat{\Pi}_{zz}$ with $\hat{v}_x$

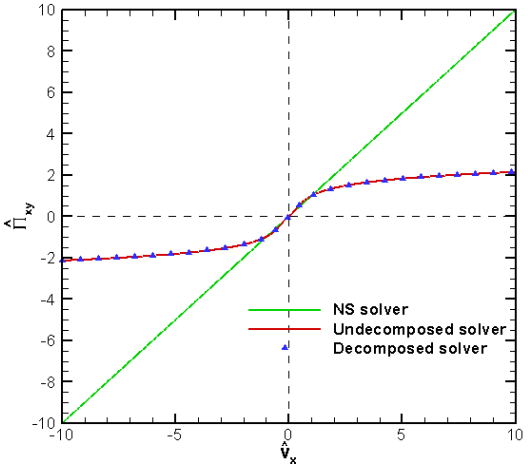

(d) Variation of $\hat{\Pi}_{xy}$ with $\hat{v}_x$

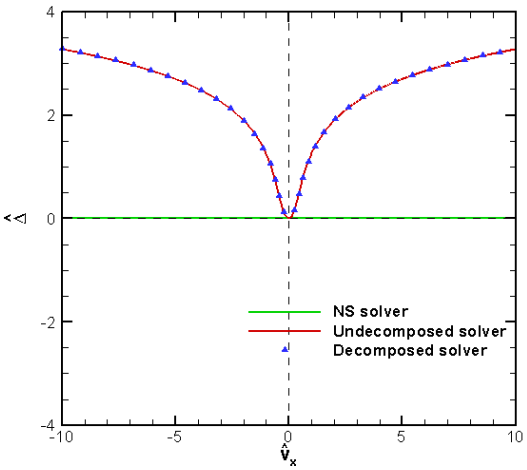

(e) Variation of $\hat{\Pi}_{xx}$ with $\hat{v}_x$

Figure 3. Constitutive relations in the $\hat{v}_x$-only problem for a diatomic gas

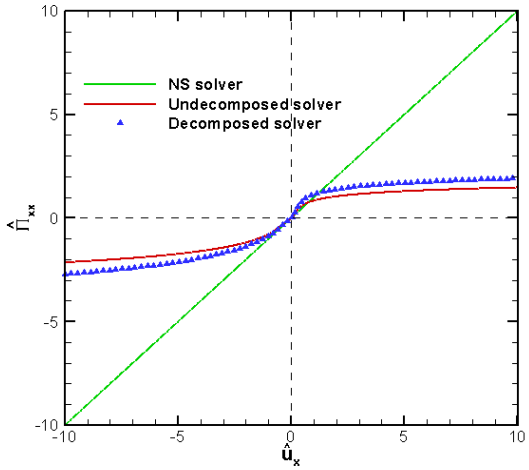

(a) Variation of $\hat{\Pi}_{xx}$ with $\hat{u}_x$

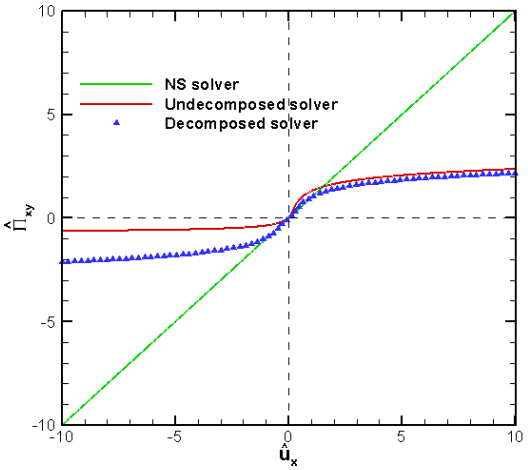

(b) Variation of $\hat{\Pi}_{xy}$ with $\hat{u}_x$

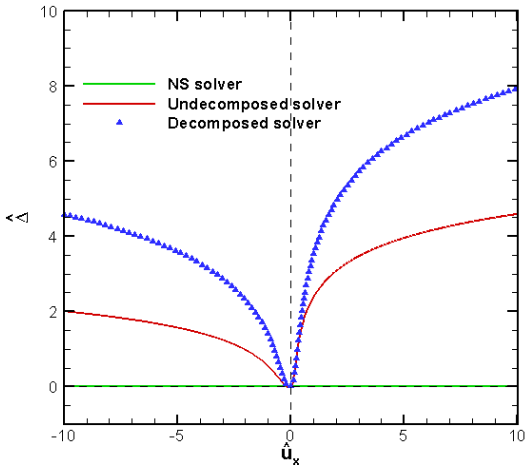

(c) Variation of $\hat{\Delta}$ with $\hat{u}_x$

Figure 4. Nonlinear constitutive relations relative to the Navier-Stokes relations in the $\hat{u}_x$-$\hat{v}_x$-only problem for a diatomic gas

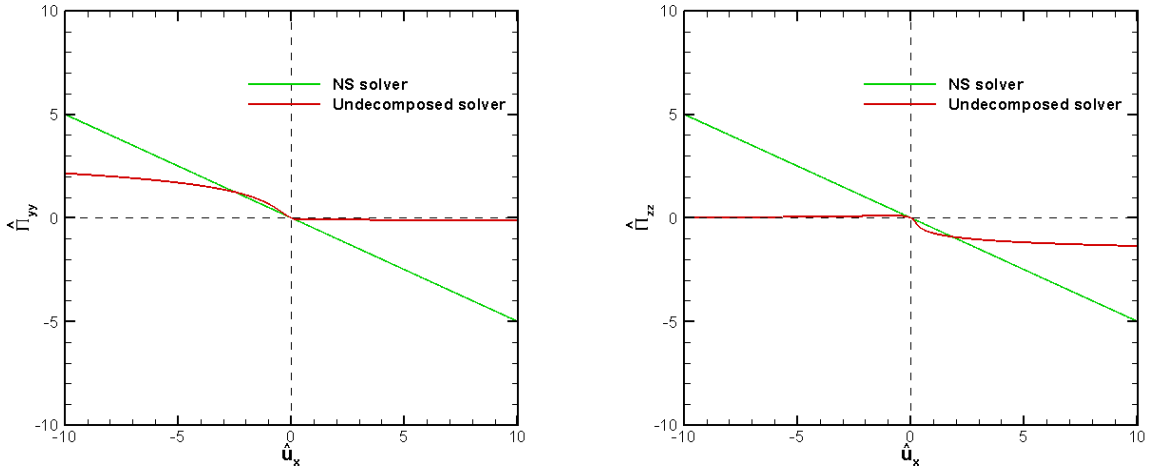

(a) Variation of $\hat{\Pi}_{yy}$ with $\hat{u}_x$ (b) Variation of $\hat{\Pi}_{zz}$ with $\hat{u}_x$

Figure 5. Nonlinear constitutive relations $\hat{\Pi}_{yy}$ (left) and $\hat{\Pi}_{zz}$ (right) with $\hat{u}_x$ computed by undecomposed solver relative to the Navier-Stokes relations in the $\hat{u}_x$ - $\hat{v}_x$ -only problem for a diatomic gas

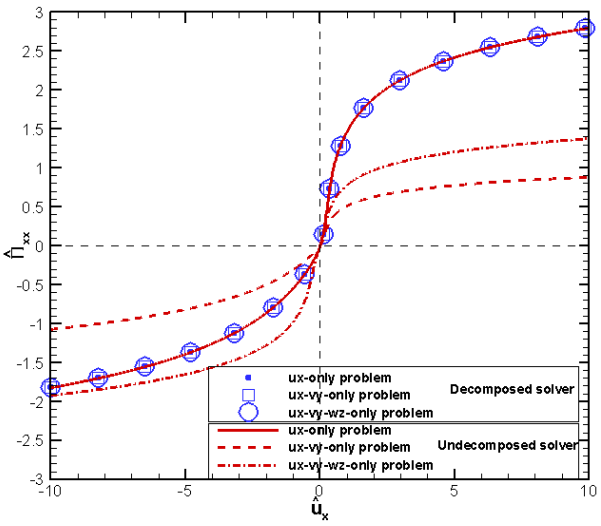

Figure 6. The nonlinear relations between $\hat{\Pi}_{xx}$ and $\hat{u}_x$ computed by decomposed and undecomposed solver in the multi-dimensional compression and expansion problem for a diatomic gas

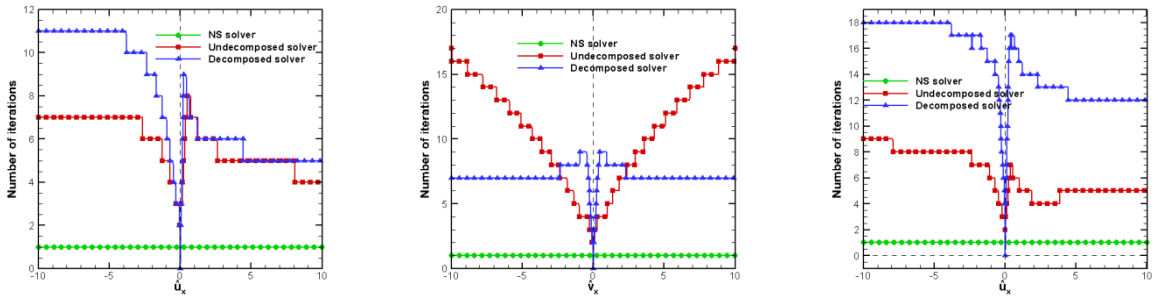

(a) $\hat{u}_x$ -only problem (b) $\hat{v}_x$ -only problem (c) $\hat{u}_x$ - $\hat{v}_x$ -only problem

Figure 7. Number of iterations for the calculation of non-conservative variables for a diatomic gas

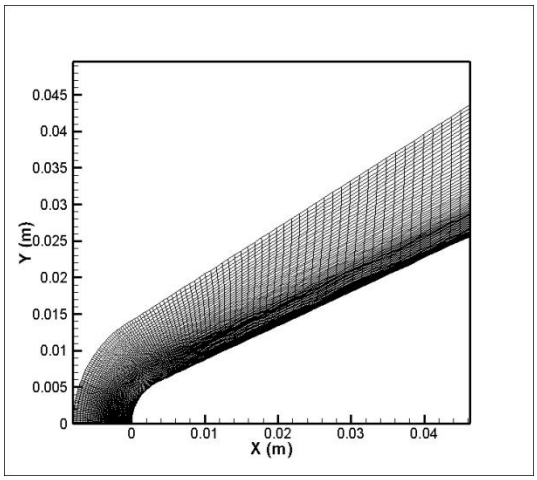

Figure 8. Structured grid of the 25^0 blunted cone's symmetrical plane

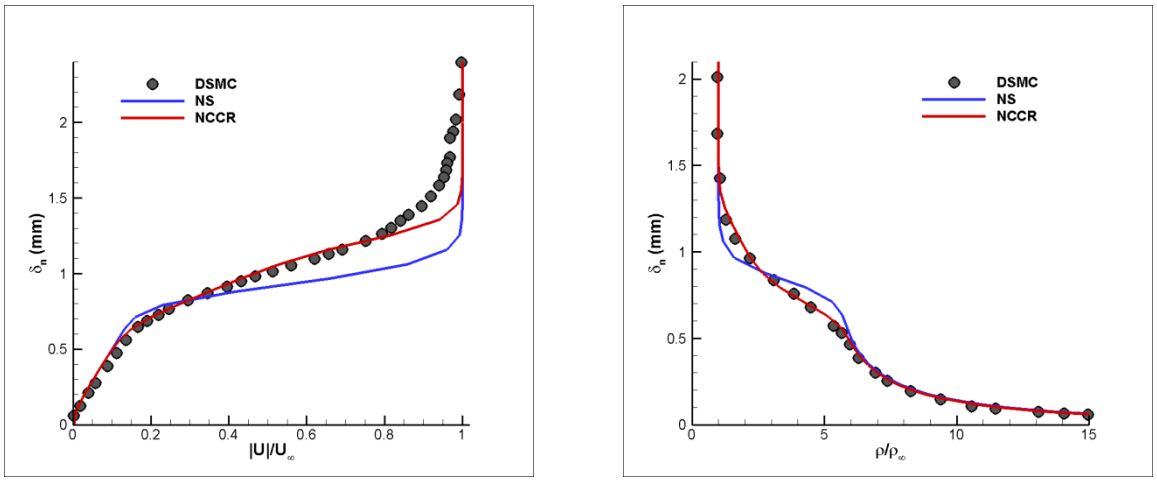

(a) Velocity (b) Density

Figure 9. Profiles along the line normal to the stagnation point

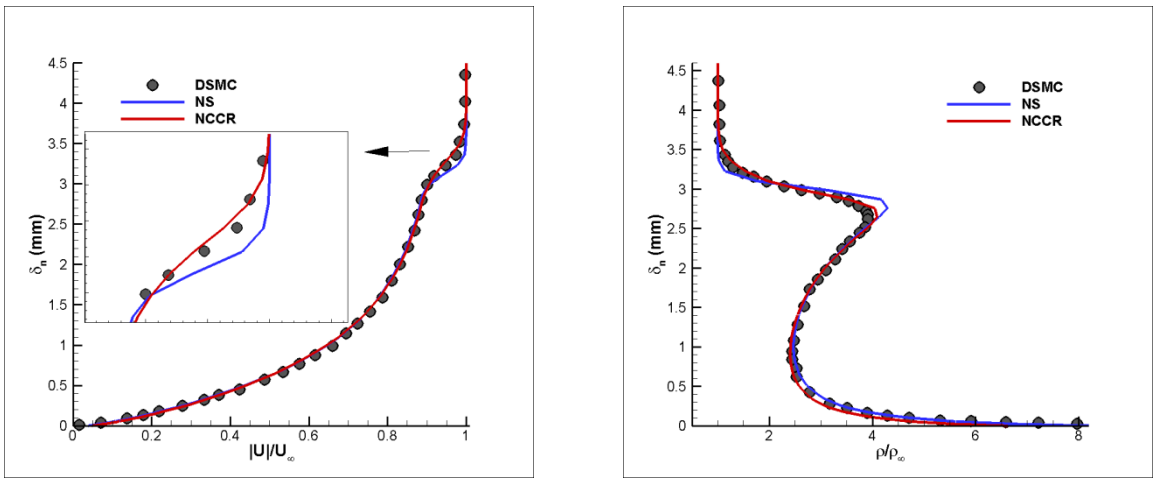

(a) Velocity (b) Density

Figure 10. Profiles along the line normal to the cone at *X*= 1.14 cm

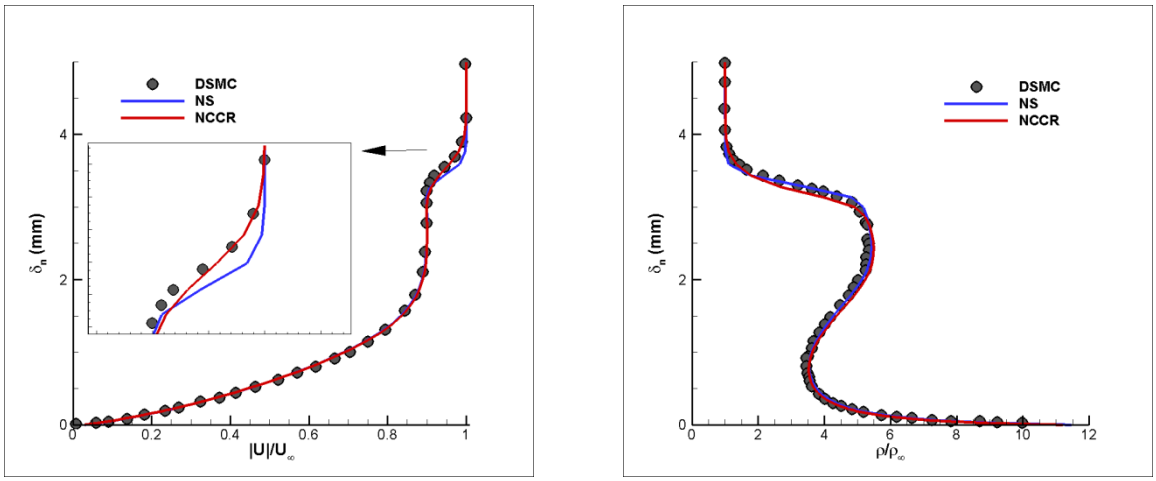

(a) Velocity (b) Density

Figure 11. Profiles along the line normal to the cone at *X*= 3.14 cm

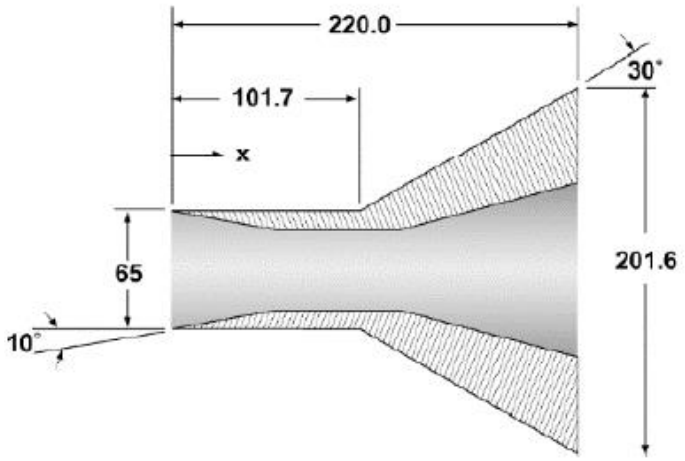

Figure 12. Schematic of hollow cylinder-flare configuration (units in millimeters)[36]

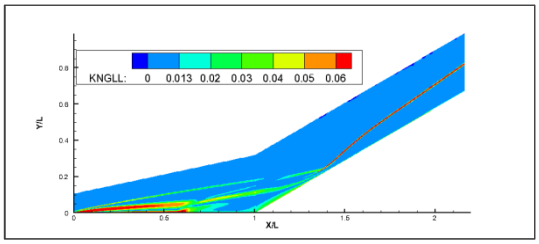

Figure 13. Gradient length local Knudsen contour

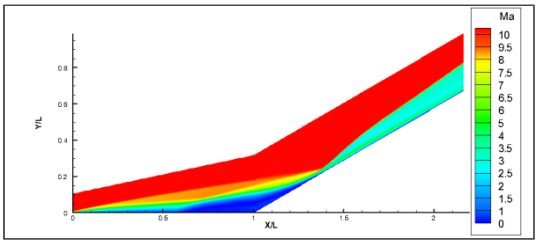

Figure 14. Mach number contour

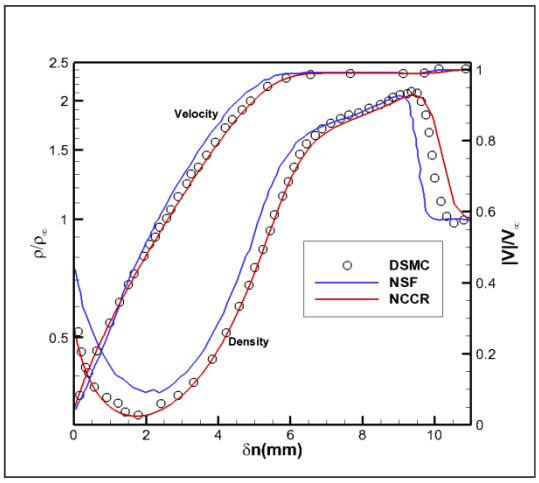

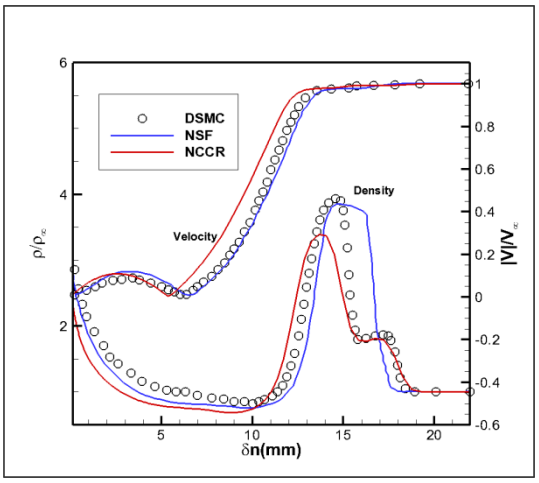

Figure 15. Density and velocity profiles along the line normal to the cylinder at x/L=0.5(left) and x/L=1(right)

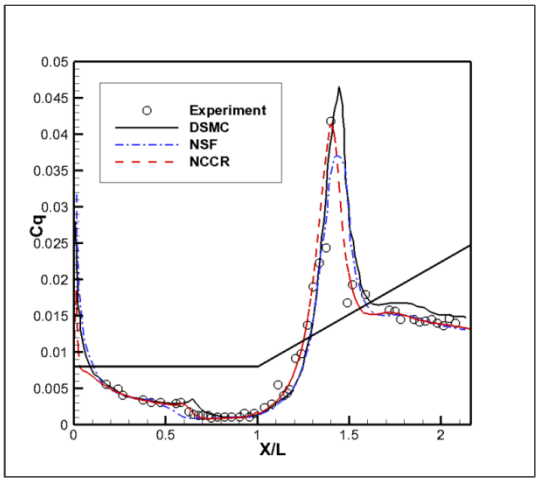

Figure 16. Comparison of surface heat flux non-dimensionalized coefficient

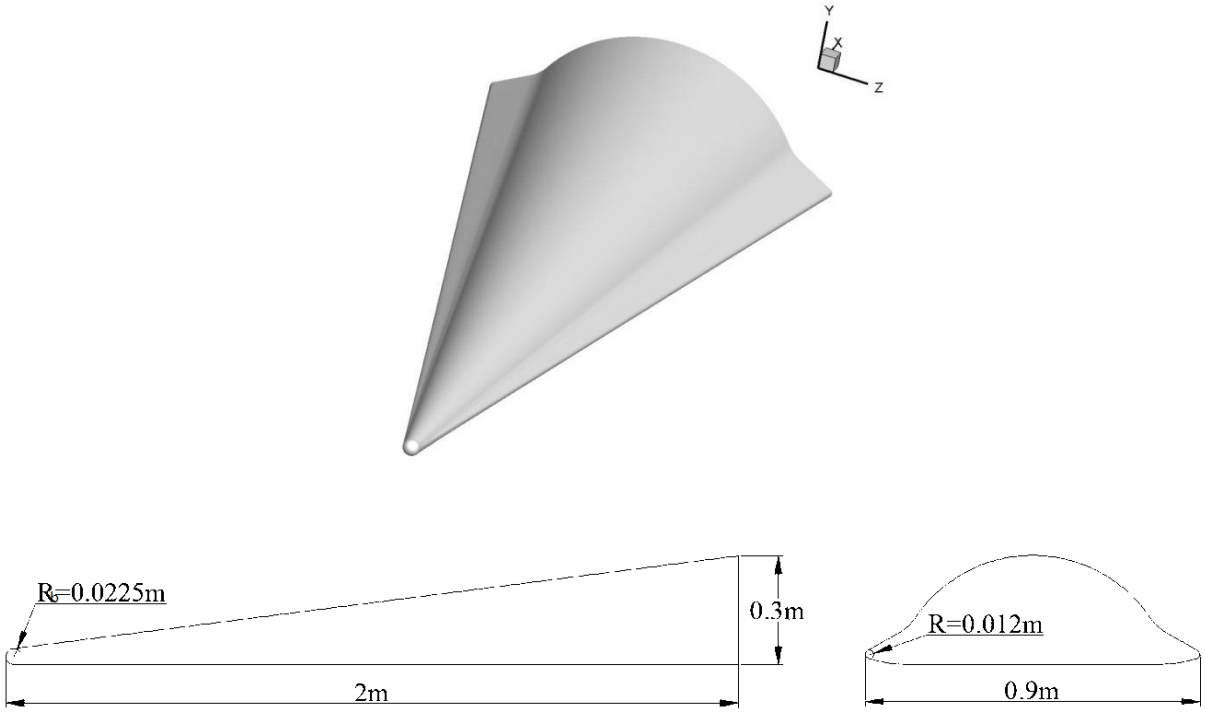

Figure 17. Schematic of the HTV-type vehicle

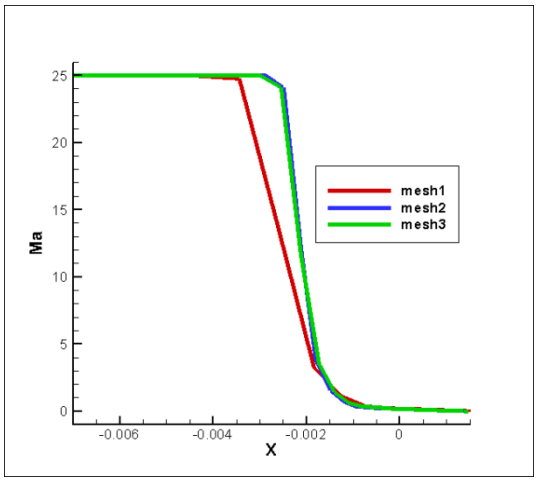

Figure 18. Mach number distributions from three different grid resolutions along the stagnation line ($Ma = 25$, $\alpha = 20^o$, $H = 50\text{km}$, $T_w = 1000\text{K}$)

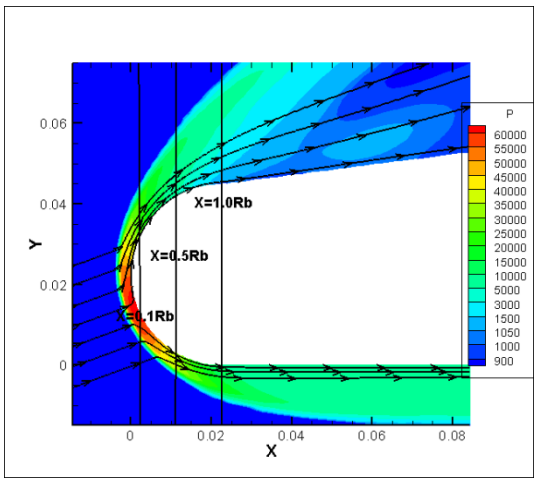

Figure 19. Local contour of pressure and streamline pattern around the sharp leading edge of the HTV-type vehicle computed by NCCR model ($Ma = 25$, $\alpha = 20^o$, $H = 50\text{km}$, $T_w = 1000\text{K}$, symmetrical plane $Z = 0$)

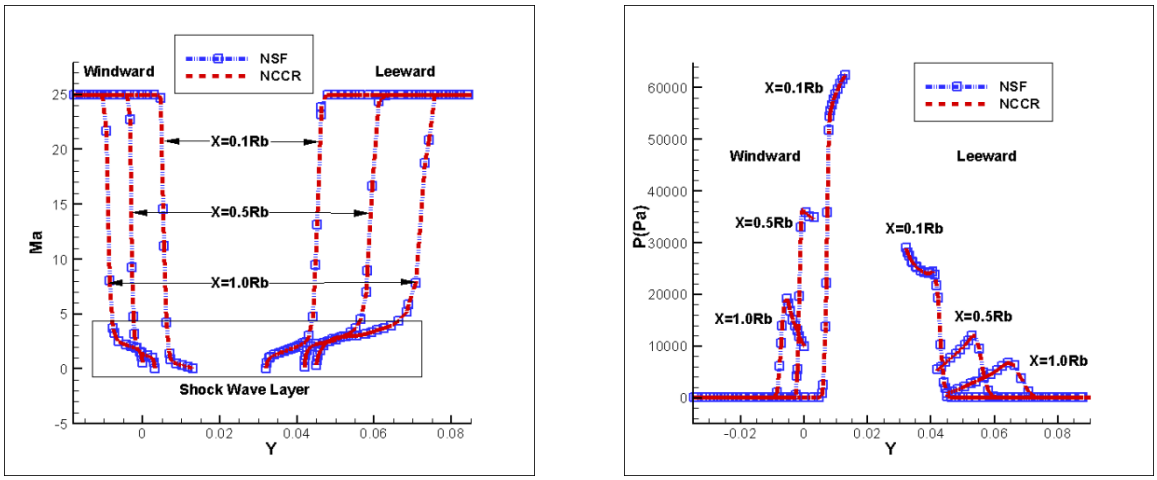

Figure 20. Windward and leeward distributions of Mach number and pressure along y direction on the symmetrical plane ($Ma = 25$, $\alpha = 20^o$, $H = 50\text{km}$, $T_w = 1000\text{K}$, symmetrical plane $Z = 0$)

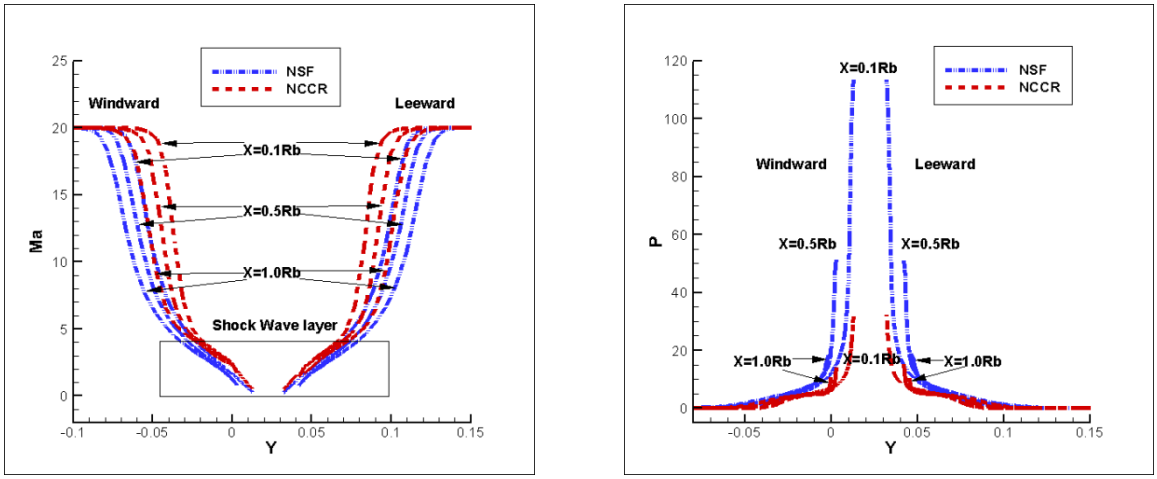

Figure 21. Windward and leeward distributions of Mach number and pressure along y direction on the symmetrical plane ($Ma = 20$, $\alpha = 0^o$, $H = 90\text{km}$, $T_w = 1000\text{K}$, symmetrical plane $Z = 0$)

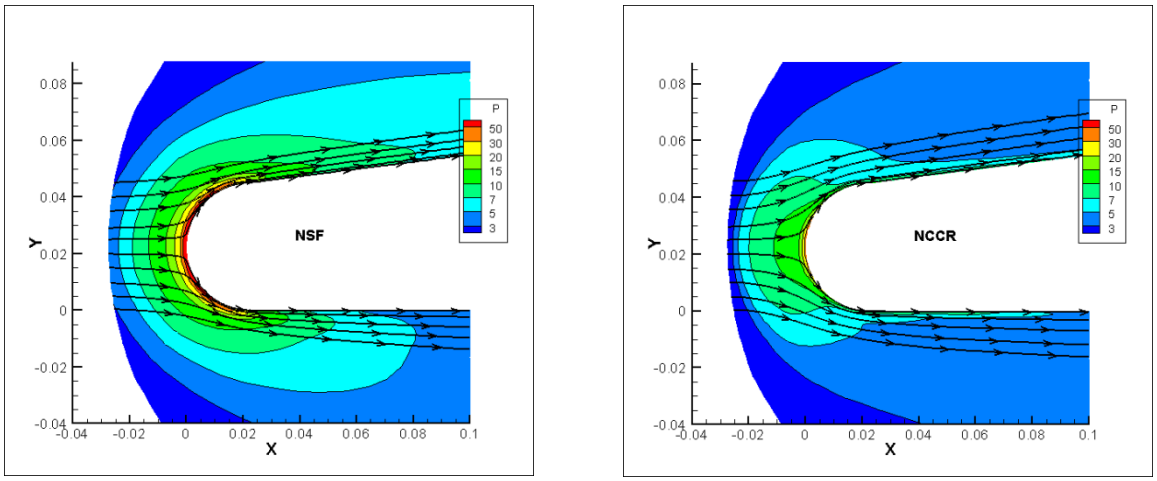

Figure 22. Local contour of pressure and streamline pattern around the sharp leading edge of the HTV-type vehicle computed by NSF and NCCR model ($Ma = 20$, $\alpha = 0^o$, $H = 90\text{km}$, $T_w = 1000\text{K}$, symmetrical plane $Z = 0$)

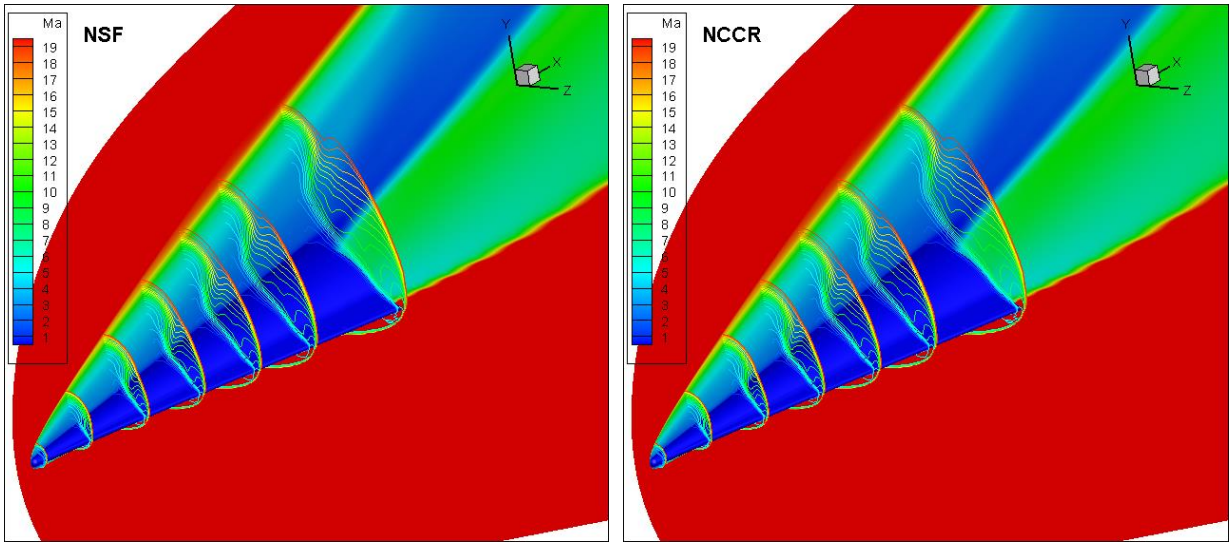

(a) $Ma = 25$, $\alpha = 20^o$, $H = 50\text{km}$, $T_w = 1000\text{K}$

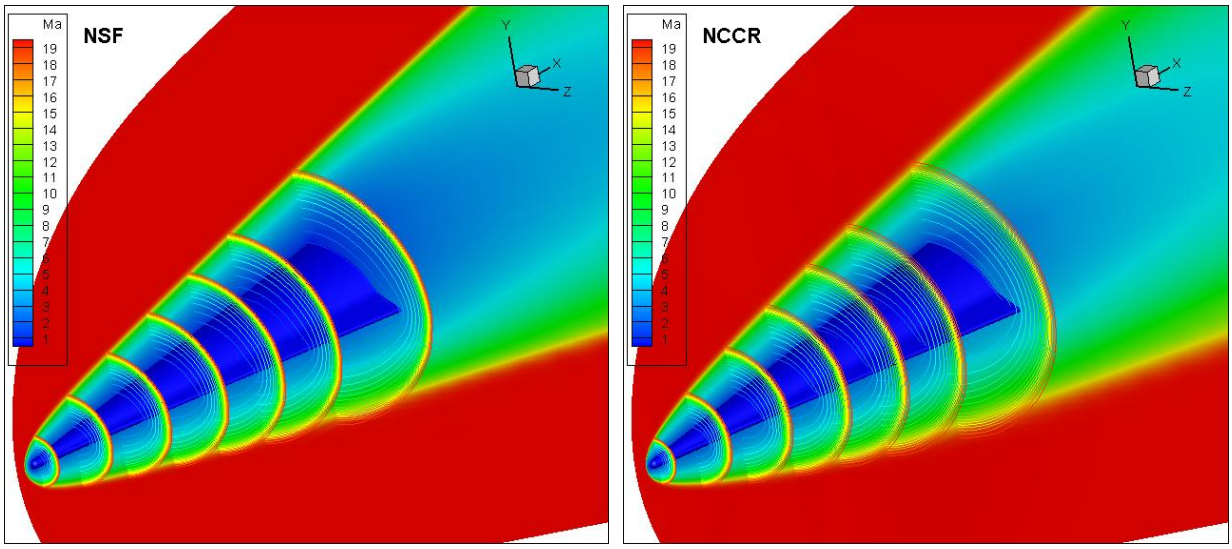

(b) $Ma = 20$, $\alpha = 0^o$, $H = 90\text{km}$, $T_w = 1000\text{K}$

Figure 23 Global contour of Mach pattern around the HTV-type vehicle computed by NSF and NCCR model at $H = 50\text{km}$ and $H = 90\text{km}$

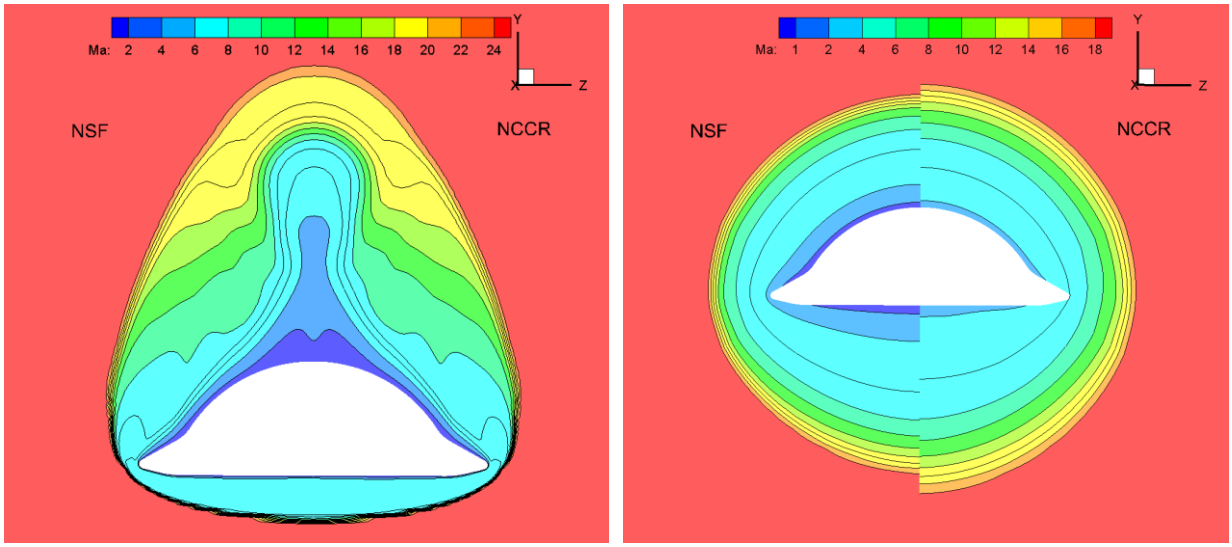

(a) $Ma = 25$, $\alpha = 20^o$, $H = 50\text{km}$, $T_w = 1000\text{K}$ (b) $Ma = 20$, $\alpha = 0^o$, $H = 90\text{km}$, $T_w = 1000\text{K}$

Figure 24 Local contour of Mach pattern on the plane of X=1.98m computed by NSF and NCCR model

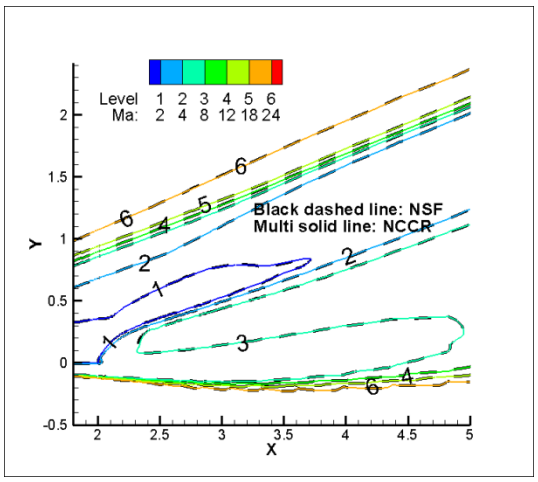

(a) $Ma = 25$, $\alpha = 20^o$, $H = 50\text{km}$, $T_w = 1000\text{K}$

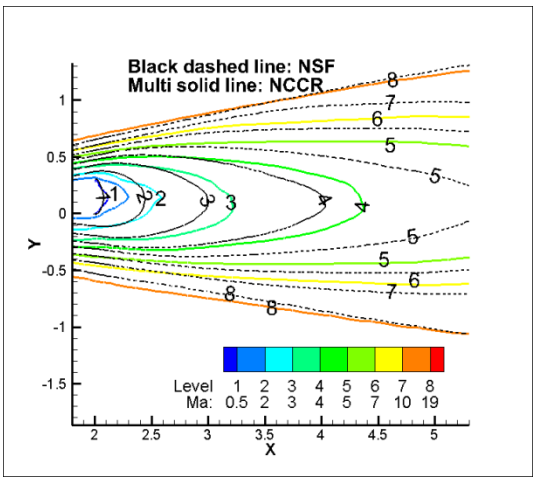

(b) $Ma = 20$, $\alpha = 0^o$, $H = 90\text{km}$, $T_w = 1000\text{K}$

Figure 25. Comparison of contour lines of after-body flow of Mach number on symmetrical plane $Z = 0$ between NS and NCCR

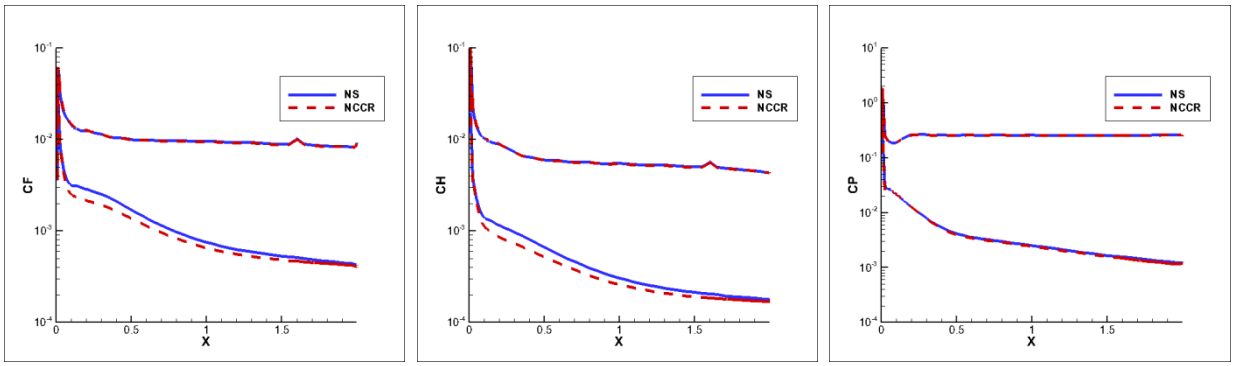

Figure 26. Comparison of surface friction, heating and pressure coefficients ($Ma = 25$, $\alpha = 20^o$, $H = 50\text{km}$, $T_w = 1000\text{K}$, symmetrical plane $Z = 0$)

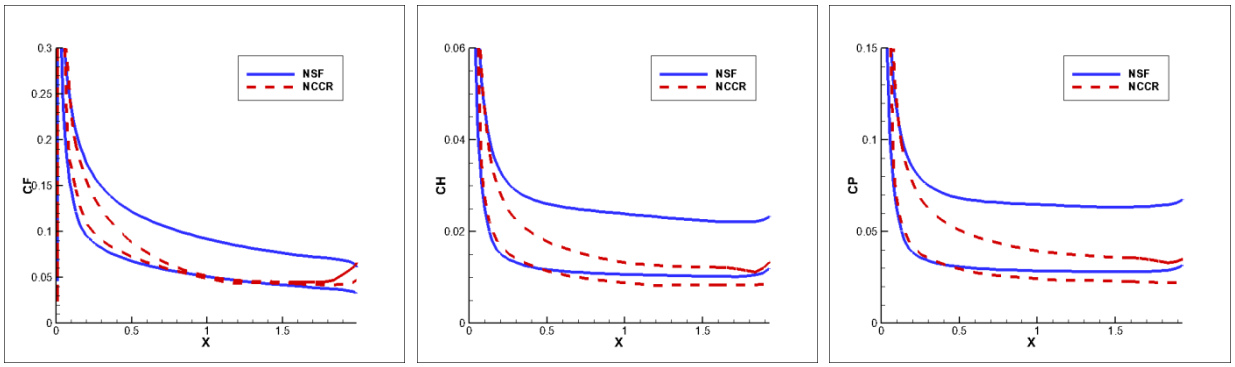

Figure 27. Comparison of surface friction, heating and pressure coefficients ($Ma = 20$, $\alpha = 0^o$, $H = 90\text{km}$, $T_w = 1000\text{K}$, symmetrical plane $Z = 0$)